Petroleum Science 23 (2026) 52–68

Contents lists available at ScienceDirect

Petroleum Science

journal homepage: www.keaipublishing.com/en/journals/petroleum-science

Original Paper

Examining the mechanisms of rebound evolution of various pore types in Longmaxi Formation shale using shale triaxial creep experiments

Yang Wang [a,b,**], Han-Yu Zhang [a,b,*], Yan-Ming Zhu [a,b], Hao-Ran Chen [a,b], Zhi-Xuan Wang [a,b], Jia-Le Li [a,b]

[a] Key Laboratory of Coalbed Methane Resources and Reservoir Formation Process, Ministry of Education, China University of Mining and Technology, Xuzhou, 221008, Jiangsu, China
[b] School of Resources and Geoscience, China University of Mining and Technology, Xuzhou, 221116, Jiangsu, China

ARTICLE INFO

Article history:
Received 14 February 2025
Received in revised form
22 May 2025
Accepted 8 September 2025
Available online 13 September 2025

Edited by Jie Hao and Xi Zhang

Keywords:
Pore rebound evolution
Organic-rich shale
Tectonic uplift
High pressure triaxial creep experiment
Sichuan Basin

ABSTRACT

The Longmaxi Formation shale in the Sichuan Basin has been affected by late-stage tectonic uplift, leading to significant differences in the pore structures of reservoir formations across various structural units and burial depths in development wells. These differences result in variations in gas content and saturation, leading to noticeable disparities in development performance and issues such as unstable production. Therefore, understanding the rebound adjustment mechanisms of pore structures in shale reservoirs is a key scientific question for uncovering the dynamic adjustment and accumulation mechanisms of shale gas. This study employs high-pressure triaxial creep experiments combined with scanning electron microscopy and fractal theory to qualitatively and quantitatively characterize various pore structures in the organic-rich shale of the Longmaxi Formation, disclosing the mechanisms and patterns of rebound response of various pore types. The results indicate that as creep pressure decreases, the rebound adjustment patterns vary among pore types. The complexity and distribution of organic matter pores initially increase and then decrease, while intergranular pores exhibit a trend of first decreasing and then increasing. Furthermore, based on microscopic evolution and changes in fractal dimension characteristics, shale pore rebound adjustment mechanisms can be broadly classified into two types: the plastic and brittle rebound adjustment pathway. This study combines theoretical analysis with experimental results to develop rebound adjustment models and response mechanisms for different pore types. This approach is essential for explaining how late-stage tectonic uplift during geological history regulates dynamic changes in shale pore structures and the process of shale gas accumulation.
© 2025 The Authors. Publishing services by Elsevier B.V. on behalf of KeAi Communications Co. Ltd. This is an open access article under the CC BY license (http://creativecommons.org/licenses/by/4.0/).

1. Introduction

In recent years, China has made significant progress in the exploration and development of deep shale gas, particularly in the Sichuan Basin, where deep shale gas resources have become a key focus for energy development (Guo et al., 2020, 2025; Zou et al., 2022, 2024; Cai et al., 2023). Scholars have gained a better understanding of the geological characteristics, reservoir conditions, and pressure coefficients of deep shale gas. It is generally accepted that deep shale gas shares similar physical parameters, such as shale thickness, TOC content, and maturity, with shallow to medium-depth shales, but exhibits higher values in terms of gas content, porosity, pressure coefficients, and in-situ stress compared to shallow and medium-depth shales (Cai et al., 2023; Sun et al., 2023; Zou et al., 2024). Furthermore, scholars have increasingly recognized the key role of quartz minerals and overpressured fluids in the occurrence of deep shale gas, positing that "quartz compressive strength preserving pores" and "overpressured fluids in the reservoir" control the development and

* Corresponding author.
** Corresponding author.
E-mail addresses: wangy89@cumt.edu.cn (Y. Wang), hyzhang9798@cumt.edu.cn (H.-Y. Zhang).
Peer review under the responsibility of China University of Petroleum (Beijing).

https://doi.org/10.1016/j.petsci.2025.09.016
1995-8226/© 2025 The Authors. Publishing services by Elsevier B.V. on behalf of KeAi Communications Co. Ltd. This is an open access article under the CC BY license (http://creativecommons.org/licenses/by/4.0/).

evolution of deep shale pores (Tenger et al., 2017; Guo et al., 2020; Cai et al., 2023). However, as exploration and development continue to expand, the focus in some production areas has shifted towards deeper formations. This shift has revealed significant differences in development outcomes among shale wells across various structural units and burial depths, along with challenges such as unstable production (Milliken et al., 2012; Gentzis, 2016; Nie et al., 2020; Li et al., 2021). An essential component of the efficient development of shale gas resources in intricate structural areas is the pore system, which acts as both a gas storage and flow space. Currently, extensive research on shale pore systems is being conducted both domestically and internationally, covering aspects such as pore types, distribution, and connectivity (Feng et al., 2020; Zhang et al., 2021; Wang et al., 2022, 2023; Chen et al., 2023; Liu et al., 2023; Sun et al., 2023; Du et al., 2024; Yang et al., 2024). Moreover, some scholars have compared the pore structure characteristics of shale at different structural positions, across various geological regions, and within different locations of the same geological structure, revealing variations in pore structure during tectonic evolution (Zhu et al., 2019; Li et al., 2021, 2024; Cheng et al., 2024a; Sun et al., 2024). The evolution of shale pore structures in deep and complex structural regions needs more investigation, even though earlier studies have offered insightful information. This is especially true when it comes to pore evolution mechanisms under geological processes like tectonic uplift.

Current research on the pore structure, morphology, adsorption capacity, and other properties of various shale pore types has yielded significant results. The findings indicate that, under the influence of tectonic forces, there are considerable differences in shale pore structure, morphological features, reservoir physical properties, and adsorption capacity (Xu et al., 2022; Xiang et al., 2022, 2024; Chai et al., 2023; Li et al., 2024). During the final tectonic uplift, the overlying strata undergo erosion and thinning, leading to a reduction in load. This results in the shale reservoir experiencing unloading, causing depressurization, expansion, or extension of the pores, a process known as pore rebound (rebound effect) (Sun, 2004; Xu et al., 2012; Zeng et al., 2016; Dong, 2018; Guo et al., 2023; Yin et al., 2023). Previous studies have compared the pore morphology, porosity, permeability, and other physical properties of shale reservoirs under different burial conditions, demonstrating that shale physical properties are highly sensitive to temperature and stress. The pore structure of shale is complex and varies under different burial conditions (Zeng et al., 2016; Long et al., 2018; Dong, 2018; Liu et al., 2020; Guo et al., 2020; Li et al., 2024; Sun et al., 2024). However, there is a lack of systematic research on the rebound effect of different pore types under tectonic uplift and its impact on reservoirs, with conflicting views among scholars. Some researchers argue that pore rebound in shale reservoirs during final tectonic uplift is a crucial factor influencing the evolution of reservoir pressure (Han et al., 2023), with microfractures and macropores undergoing significant changes in response to reservoir pressure (Guo et al., 2023; Yin et al., 2023). Other studies suggest that pore volume rebound in shale has a minimal effect on the internal pressure of the reservoir (Zhang et al., 2023; Sun et al., 2024), while under tectonic uplift, the pore volume and specific surface area of micropores and mesopores increase significantly, further affecting the reservoir's methane adsorption capacity (Zeng et al., 2016; Xu et al., 2022; Sun et al., 2024). In addition, although different pore types generally show an increase in volume, number, and complexity of pore structure under tectonic uplift (Xu et al., 2022; Cheng et al., 2024a; Guo et al., 2023; Yu et al., 2024), the rebound adjustment pathways of organic matter and mineral pores during final tectonic uplift exhibit significant differences. This limits the understanding of the shale reservoir's response mechanism to tectonic uplift, a fundamental issue in shale gas research.

The purpose of this study is to identify the mechanisms and characteristics of the rebound response of shale pores under late-stage tectonic uplift. First, a high-pressure triaxial test system was used to perform compression recovery on shale under varying confining pressure conditions. Scanning electron microscopy (Ar-SEM), fractal theory analysis, and argon ion beam polishing were used to qualitatively and quantitatively analyze the organic matter pores, intergranular pores, and microfractures in creep-deformed shale samples. Based on the observed evolution patterns of organic matter pores, intergranular pores, and microfractures in mudstone under varying confining pressures, this study reveals the rebound response mechanisms of different pore types in mudstone during late-stage tectonic uplift. In contrast to earlier research on the development of mudstone pore structures, this study is innovative in that it suggests that mudstone pore structures have an innate propensity for rebound recovery in addition to removing the impact of non-deformation factors on pore structure re-bound recovery. Mudstone triaxial creep experiments were used to obtain the shale samples for this study under various burial depth conditions. Additionally, the samples were freshly collected from outcrops, ensuring that they had identical initial pore structures and organic geochemical characteristics before the triaxial creep experiments. Additionally, the initial pore structure characteristics had already undergone rebound recovery following the most recent tectonic uplift, ensuring that any differences in pore structure between shale samples before and after the creep experiments can be attributed to the rebound adjustment of the pore structure.

The results of this work address this fundamental scientific question by offering a thorough examination of how the pore structure of organic-rich shale reacts and modifies during rebound under the impact of the most recent tectonic uplift. This understanding is essential for explaining how the most recent tectonic uplift during geological history regulates dynamic changes in the pore architecture of shale and the accumulation of shale gas. Based on these insights, the research findings are expected to provide crucial support and a foundation for assessing shale gas resource potential and ensuring its efficient development in complex geological settings.

2. Background geology and sample gathering

2.1. Geological overview

The Sichuan Basin is situated on the western margin of the Upper Yangtze Platform, forming a composite basin that integrates a large Paleozoic cratonic basin with a Meso-Cenozoic foreland basin. The western side of the basin is bordered by the Emeishan-Liangshan block fault zone and the Longmen Shan marginal fold-thrust belt. The northern boundary is marked by the Micang Shan platform uplift and the Dabashan marginal fold-thrust belt, the eastern boundary by the Loushan-Bamian Shan fold-thrust belt, and the southern part gradually transitions into the Sichuan-Yunnan uplift zone (Fig. 1(a)) (Meng et al., 2005; Gu et al., 2021; Liu et al., 2021).

Within the Sichuan Basin, the Eastern Sichuan High and Steep Fold Belt and the Southern Sichuan Low and Gentle Fold Belt are categorized as secondary tectonic units (Fig. 1(a)) (Liu et al., 2012; Wei et al., 2019). Every shale sample used in this investigation came from the Sichuan Basin's eastern and southern areas (marked in Fig. 1(a)). The strata in the southern Sichuan study region are almost east-west orientated, and the superposition of north-south and east-west trending folds and faults characterizes

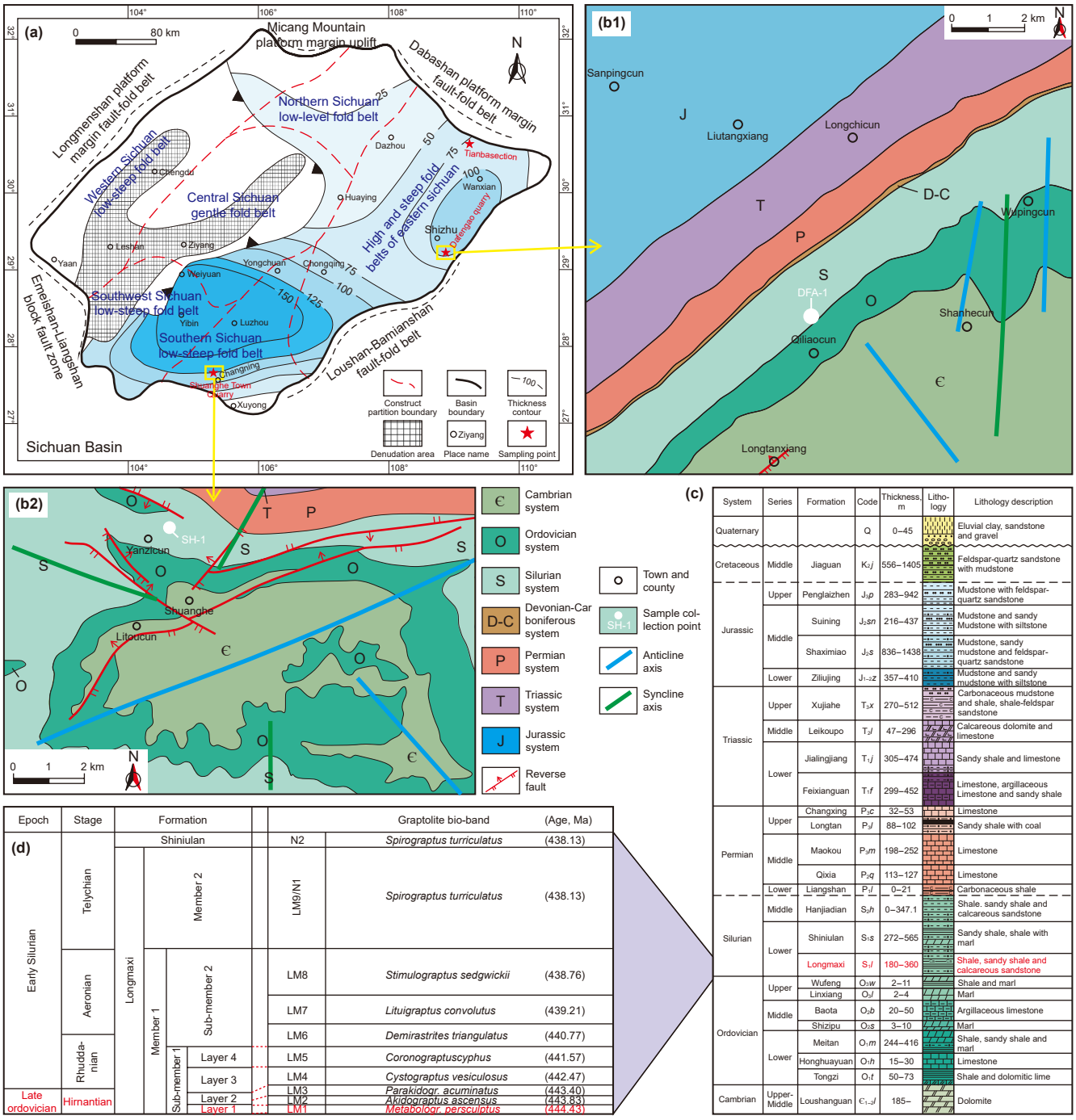

System	Series	Formation	Code	Thickness, m	Lithology description
Quaternary			Q	0–45	Eluvial clay, sandstone and gravel
Cretaceous	Middle	Jiaguan	K_2j	556–1405	Feldspar-quartz sandstone with mudstone
Jurassic	Upper	Penglaizhen	J_3p	283–942	Mudstone with feldspar-quartz sandstone
	Middle	Suining	J_2sn	216–437	Mudstone and sandy Mudstone with siltstone
		Shaximiao	J_2s	836–1438	Mudstone, sandy mudstone and feldspar-quartz sandstone
	Lower	Ziliujing	J_1–$_2z$	357–410	Mudstone and sandy mudstone with siltstone
Triassic	Upper	Xujiahe	T_3x	270–512	Carbonaceous mudstone and shale, shale-feldspar sandstone
	Middle	Leikoupo	T_2l	47–296	Calcareous dolomite and limestone
	Lower	Jialingjiang	T_1j	305–474	Sandy shale and limestone
		Feixianguan	T_1f	299–452	Limestone, argillaceous Limestone and sandy shale
Permian	Upper	Changxing	P_3c	32–53	Limestone
		Longtan	P_3l	88–102	Sandy shale with coal
	Middle	Maokou	P_2m	198–252	Limestone
		Qixia	P_2q	113–127	Limestone
	Lower	Liangshan	P_1l	0–21	Carbonaceous shale
Silurian	Middle	Hanjiadian	S_2h	0–347.1	Shale. sandy shale and calcareous sandstone
	Lower	Shiniulan	S_1s	272–565	Sandy shale, shale with marl
		Longmaxi	S_1l	180–360	Shale, sandy shale and calcareous sandstone
Ordovician	Upper	Wufeng	O_3w	2–11	Shale and marl
		Linxiang	O_3l	2–4	Marl
	Middle	Baota	O_2b	20–50	Argillaceous limestone
		Shizipu	O_2s	3–10	Marl
	Lower	Meitan	O_1m	244–416	Shale, sandy shale and marl
		Honghuayuan	O_1h	15–30	Limestone
		Tongzi	O_1t	50–73	Shale and dolomitic lime
Cambrian	Upper-Middle	Loushanguan	$\epsilon_{1-3}l$	185–	Dolomite

Epoch	Stage	Formation			Graptolite bio-band	(Age, Ma)
Early Silurian	Telychian	Shiniulan			N2 *Spirograptus turriculatus*	(438.13)
		Longmaxi	Member 2		LM9/N1 *Spirograptus turriculatus*	(438.13)
	Aeronian		Member 1	Sub-member 2	LM8 *Stimulograptus sedgwickii*	(438.76)
					LM7 *Lituigraptus convolutus*	(439.21)
					LM6 *Demirastrites triangulatus*	(440.77)
	Rhuddanian			Sub-member 1 Layer 4	LM5 *Coronograptuscyphus*	(441.57)
				Layer 3	LM4 *Cystograptus vesiculosus*	(442.47)
					LM3 *Parakidogr. acuminatus*	(443.40)
Late ordovician	Hirnantian			Layer 2	LM2 *Akidograptus ascensus*	(443.83)
				Layer 1	LM1 *Metabologr. persculptus*	(444.43)

Fig. 1. **(a)** Tectonic subdivision of the Sichuan Basin. **(b1)** and **(b2)** Maps of sample collection in Shanghe area and Dafengao area, respectively. **(c)** Strata diagram. **(d)** Comprehensive stratigraphic column of the Wufeng–Longmaxi Formation of the study area (modified from Shi et al., 2021; Cheng et al., 2022 and Cheng et al., 2024a).

the structural pattern (Fig. 1(b2)) (Cheng et al., 2022; Cheng et al., 2024a). In contrast, the strata in the eastern Sichuan study area are primarily oriented NE-SW, with structures predominantly consisting of nearly north-south trending folds (Fig. 1(b1)).

The Cambrian to Jurassic strata in the research area are well formed, with the exception of the Devonian, Carboniferous, Cretaceous, Paleogene, and Neogene systems (Fig. 1(c)). The Lower Silurian Longmaxi Formation, which is widely disclosed in the study area, is one of the primary target strata for shale gas exploration and production in the Sichuan Basin. According to the isopach map, the Longmaxi shale generally extends outward from two central high-thickness areas: southern Sichuan's Luzhou and eastern Sichuan's Shizhu. In these high-thickness zones, the black shale exceeds 100 m in thickness, providing a material foundation for shale gas accumulation (Fig. 1(a)). There are essentially two parts to the Longmaxi Formation. The bottom portion, referred to as the First Member (Long 1), has a thickness of roughly 50–135 m and is composed of siliceous, dark gray siltstone, and organic-rich black carbonaceous shale. The upper section, known as the Second Member (Long 2), consists of gray or yellow-green shale interbedded with siltstone or marlstone, with a lower content of graptolites and a thickness ranging from 130 to 225 m (Shi et al., 2021;

Cheng et al., 2024a). The Longmaxi Formation can be broadly categorized into three subsections: SQ1, SQ2, and SQ3 based on its stratigraphic evolution (Shi et al., 2021). The large shale samples collected for this study were all taken from the First Submember of the Longmaxi Formation, which primarily comprises black graptolite shale (Fig. 1(d)).

2.2. Sample information and triaxial creep experiment

Investigating the mechanisms of the pore structure and rebound response characteristics in organic-rich shale under the impact of the most recent tectonic uplift is the primary goal of this study (Fig. 2(a)). Large samples of organic-rich black graptolite shale from the eastern and southern Sichuan structural zones' Lower Silurian Longmaxi Formation were gathered for the study. Systematic shale triaxial creep experiments were conducted under different creep pressure conditions to simulate the original geological burial state (Fig. 2(b)). Samples of deformed shale were collected during this procedure (Fig. 2(a)). On this basis, the study employed a combination of Ar-SEM technology and quantitative analysis with Image Pro Plus (IPP) software to examine the microstructural and morphological deformation characteristics of different pore types. This approach ultimately revealed the rebound response mechanisms of various pore types (pores of organic substances and intergranular) in shale under the influence of the most recent tectonic uplift (Fig. 2(d)).

First, all undeformed shale samples used in the triaxial creep experiments were newly collected large outcrop samples from the eastern and southern regions of the Sichuan Basin. This was carried out in order to precisely describe the evolution characteristics and mechanisms of the shale pore rebound response and to guarantee that the shale samples had the same initial conditions before the experimental deformation. The specific locations are the Dafeng'ao Tunnel open stone dump in Shizhu County, Chongqing, Eastern Sichuan; the Tianba section in Wuxi County, Chongqing, Eastern Sichuan; and the Shuanghe open quarry in Changning County, Yibin, Southern Sichuan (Fig. 1(a)). Due to tunnel expansion and quarry excavation, both sites provided a large number of fresh, intact shale samples (Fig. 2(c)). The shale samples collected in this study are from the LM 1 biozone of the Lower Silurian Longmaxi Formation, and their physical and mechanical properties are presented in Table 1.

Secondly, to guarantee consistent geochemical and early pore structure properties, shale core samples were made from the identical sizable fresh outcrop samples for every univariate control group. To prevent water-clay mineral interactions in the shale cores during experimental deformation (Chaturvedi and Sharma, 2022; Cheng et al., 2024b), a low-speed dry diamond wire cutting pattern was used to prepare standard cylindrical specimens (100 mm in height, 50 mm in diameter).

This study employed a high-pressure geotechnical triaxial test system to conduct mechanical triaxial creep experiments under various confining pressure conditions. The system can achieve temperatures ranging from −20 to 800 °C, confining pressures from 0 to 30 MPa, and axial stresses up to 1.6 GPa (Fig. 2(b)). Palm oil was used as the confining pressure medium. Compared to an air medium, a solid medium offers greater rigidity, better simulating in-situ formation conditions and helping to maximize the integrity of the experimental samples. The shale triaxial creep experiment consists of three stages: a synchronous preloading confining pressure stage (simulating the burial process) with a loading rate of 5000 kPa/h; a confining pressure holding stage (simulating the underground preservation state) with a creep duration of 72 h; and a rapid confining pressure unloading stage. A detailed description of the deformation system and the loading/unloading process can be found in the supplementary materials, with the experimental deformation data of the shale samples and the final results presented in Table 2 (see Table 3).

2.3. Method of fractal calculation

FE-SEM images are typically grayscale, with pores and minerals distinguishable based on different grayscale values. To extract pores from the grayscale image, a thresholding segmentation method is commonly used, which has been widely applied to analyze the development characteristics of irregular pores in heterogeneous solids such as shale and coal (Feng et al., 2019; Liu et al., 2023). The choice of threshold is crucial for the accuracy of pore selection. To minimize errors, the threshold range is determined by adjusting the contrast, saturation, and other properties of the pore image, thereby accurately delineating the pores for the optimal selection result (Fig. 2(d)). Therefore, assuming $g(x, y)$ represents the grayscale value at a specific point in the image, the formula for binarizing the image is as follows (Voss et al., 1991; Feng et al., 2019):

$$g(x,y) = f(x) = \begin{cases} 0, f(x,y) > T \\ 1, f(x,y) \le T \end{cases} \quad (1)$$

Here, $g\ (x,\ y)$ represents the binarized image obtained after processing, and T is the determined threshold value.

This study calculates the fractal parameters of different types of shale pores using the Voss fractal model based on two-dimensional image data. If the pore morphology in the sample images exhibits fractal characteristics, the relationship between pore area, equivalent perimeter, and fractal dimension is as follows (Voss et al., 1991):

$$\log P = (D/2) \log A + C \quad (2)$$

Here, P represents the equivalent perimeter of the pore; A denotes the pore area; C is a constant; and D is the fractal dimension corresponding to the pore, as derived from the 2D image analysis.

The structural parameters of different pore types (equivalent perimeter and pore area) are subjected to least squares linear fitting in a double-logarithmic coordinate system, yielding the slope of the line (Fig. 2(d)). The fractal dimension (D) of the different pore types in shale is then calculated using the following formula:

$$D = 2 \times K \quad (3)$$

Here, K represents the slope of the fitted line for the equivalent pore perimeter and pore area on the double-logarithmic plot. The fractal dimension (D) of shale pores ranges from 1 to 2, where 2 represents a completely irregular or rough surface, and 1 represents a completely smooth surface (Sun et al., 2016; Feng et al., 2019; Liu et al., 2023).

3. Results

3.1. Morphological traits and the rule of evolution of organic matter pores in shale

The organic matter in the shale samples may be roughly classified into two types: locally aggregated organic matter and diffused organic matter, according to this study's observations of the materials using SEM both before and after experimental deformation. Aggregated organic matter is primarily distributed between brittle minerals, particularly between quartz particles (Fig. 3(a)–(l)). Dispersed organic matter primarily exists in two forms: coexisting with pyrite or combining with clay minerals to form “organic-clay complexes” (Fig. 3(c) and (e)). Observational statistics indicate that the Longmaxi Formation shale

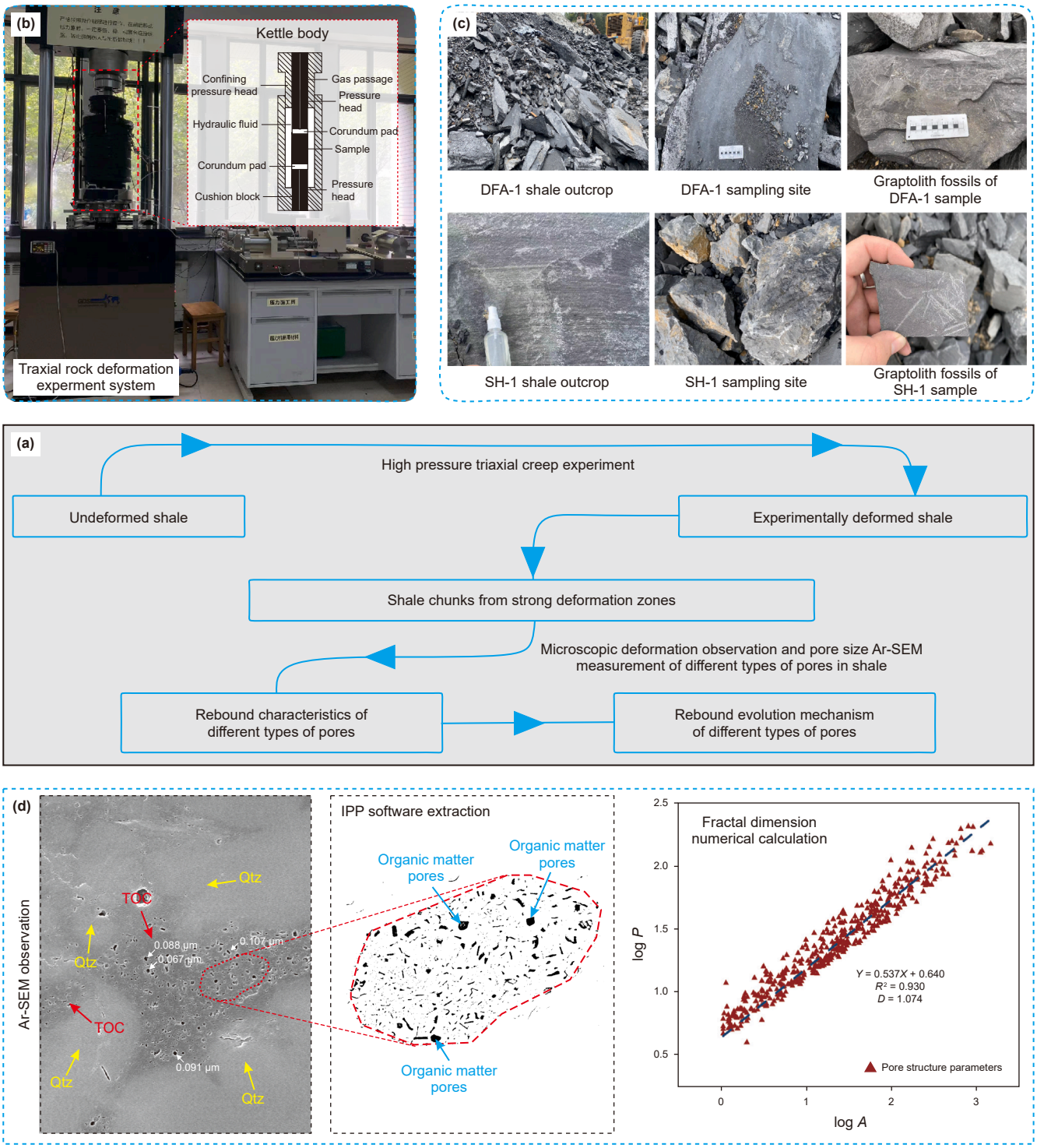

Fig. 2. Flowchart of research process and methodology. Notes: Qtz = Quartz, OM = Organic matter.

Table 1
Physical property parameters of Longmaxi Formation shale samples.

Sample	TOC, %	Average VR_{eqv}, %	v^G–v^D	Mineral content, %				
				Quartz	Feldspar	Clay	Carbonate	Pyrite
TB-1	7.8	3.04	265.35	79.2	4.1	16.7	0	0
SH-1	2.79	3.53	273.68	27.7	9	40.1	22.6	0
DFA-1	6.29	3.49	274.42	66.0	6.7	16.6	5.6	5.1

Table 2
Sample parameters, experimental conditions, and experimental results of the triaxial creep test on longmaxi shale.

Sample	Diameter before experiment, mm	Height before experiment, mm	Confining pressure, MPa	Creep time, h	Height after experiment, mm	Diameter after experiment, mm	Maximum axial displacement, mm	Axial strain, % [(a)]	Maximum radial displacement, mm	Radial strain, % [(b)]
TB-11	50.13	99.64	10	72	50.08	99.49	0.3209	0.322	0.0794	0.158
TB-1-2	50.11	100.13	20	72	50.07	100.06	0.1302	0.130	0.0446	0.089
DFA-1-1	50.14	100.16	10	72	50.12	100.14	0.254	0.254	0.1068	0.213
DFA-1-2	50.13	100.11	20	72	49.97	100.03	0.335	0.335	0.0026	0.005
SH-1-1	50.08	99.87	10	72	50.05	99.63	0.280	0.280	0.0618	0.123
SH-1-2	50.05	100.36	20	72	50.05	99.98	0.66	0.658	0.1921	0.384

[(a)] Axial strain, % = Maximum axial displacement/Height before experiment.
[(b)] Radial strain, % = Maximum radial displacement/Diameter before experiment.

Table 3
The calculated fractal dimensions of organic matter pores and intergranular pores under different confining pressure.

Sample number	Pore type	Statistical magnitude	Fractal dimension	Correlation coefficient
SH-1	Intergranular pores (20 MPa)	528	1.454	0.933
	Intergranular pores (10 MPa)	633	1.174	0.876
	Intergranular pores (0 MPa)	457	1.318	0.832
DFA-1	Organic matter pore (20 MPa)	210	1.032	0.896
	Organic matter pore (10 MPa)	233	1.348	0.966
	Organic matter pore (0 MPa)	389	1.066	0.87
TB-1	Organic matter pore (20 MPa)	485	1.074	0.930
	Organic matter pore (10 MPa)	551	1.082	0.724
	Organic matter pore (0 MPa)	512	1.050	0.928
	Intergranular pores (20 MPa)	459	1.220	0.901
	Intergranular pores (10 MPa)	262	1.178	0.932
	Intergranular pores (0 MPa)	181	1.222	0.906

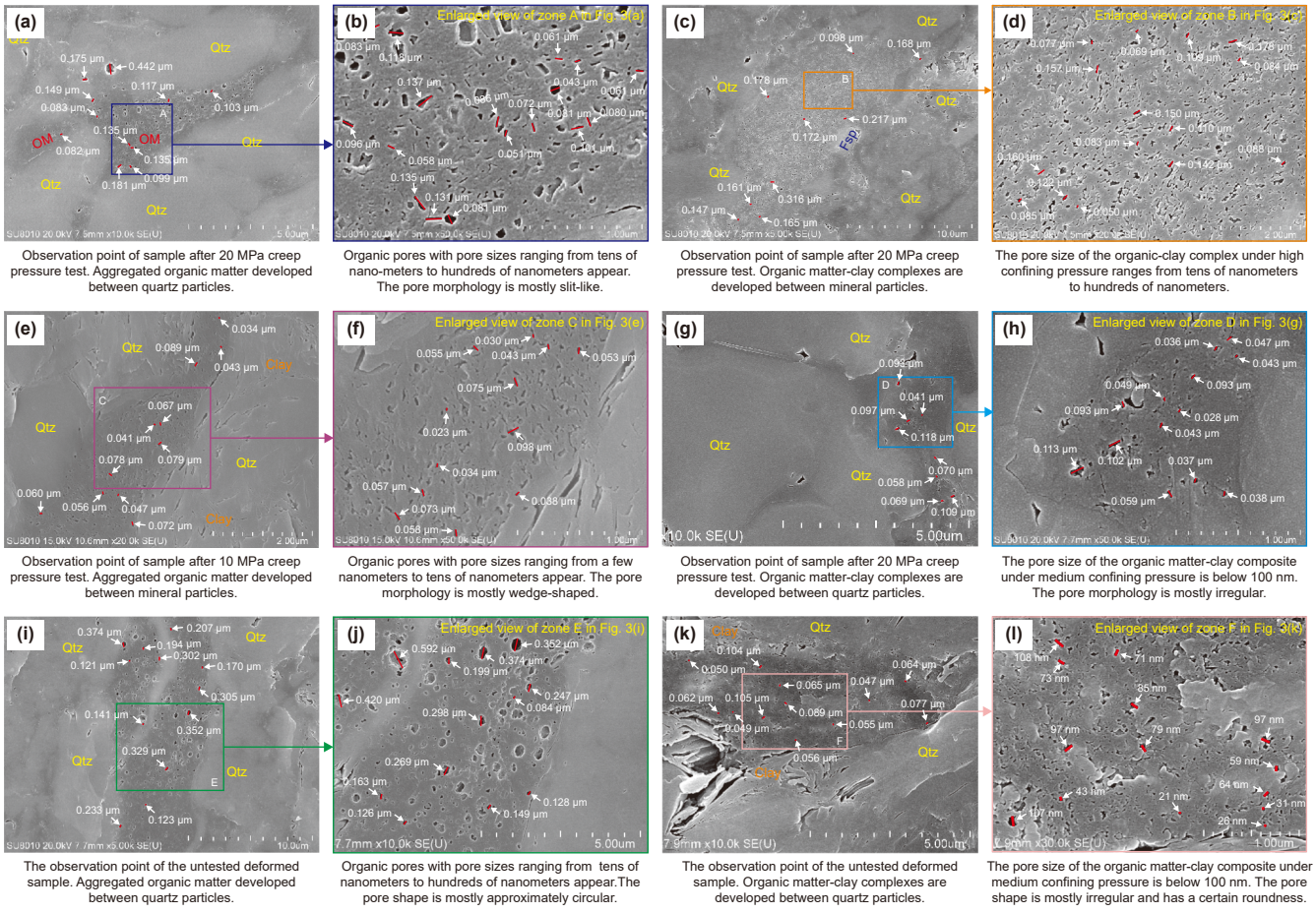

Observation point of sample after 20 MPa creep pressure test. Aggregated organic matter developed between quartz particles.

Organic pores with pore sizes ranging from tens of nano-meters to hundreds of nanometers appear. The pore morphology is mostly slit-like.

Observation point of sample after 20 MPa creep pressure test. Organic matter-clay complexes are developed between mineral particles.

The pore size of the organic-clay complex under high confining pressure ranges from tens of nanometers to hundreds of nanometers.

Observation point of sample after 10 MPa creep pressure test. Aggregated organic matter developed between mineral particles.

Organic pores with pore sizes ranging from a few nanometers to tens of nanometers appear. The pore morphology is mostly wedge-shaped.

Observation point of sample after 20 MPa creep pressure test. Organic matter-clay complexes are developed between quartz particles.

The pore size of the organic matter-clay composite under medium confining pressure is below 100 nm. The pore morphology is mostly irregular.

The observation point of the untested deformed sample. Aggregated organic matter developed between quartz particles.

Organic pores with pore sizes ranging from tens of nanometers to hundreds of nanometers appear.The pore shape is mostly approximately circular.

The observation point of the untested deformed sample. Organic matter-clay complexes are developed between quartz particles.

The pore size of the organic matter-clay composite under medium confining pressure is below 100 nm. The pore shape is mostly irregular and has a certain roundness.

Fig. 3. Organic matter pore characteristics of longmaxi shale at different burial depths.

predominantly contains aggregated organic matter, followed by organic-clay complexes, with the lowest content being organic matter coexisting with pyrite. The pores within aggregated organic matter between mineral particles are primarily sponge-like, with elliptical, nearly circular, or slit-like shapes. Most aggregated organic matter pores typically range from tens to several hundred nanometers in diameter (Fig. 3(b)–(h) and (j)). Secondly, the pore shapes in organic-clay complexes are mostly slit-like and irregular. These pores are relatively small, typically ranging from a few nanometers to several tens of nanometers, with some reaching up to several hundred nanometers (Fig. 3(d)–(f) and (l)).

The growth of organic matter pores in the shale samples varied somewhat after going through several creep deformation tests. Organic matter pores formed between brittle mineral particles exhibited no significant change under various pressure conditions; they did not undergo identifiable deformation or alteration, and their shapes remained elliptical or nearly circular (Fig. 3(b)–(j) and (h)). In contrast, the pores within the 'organic-clay complexes' experienced intense compression under high creep pressure (20 MPa), causing the complexes to become tightly compacted. As a result, the pores within these complexes closed or contracted, forming numerous slit-like and directionally oriented organic matter pores (Fig. 3(d)). As the triaxial creep pressure decreases, the number of pores within the 'organic-clay complexes' increases, indicating that under moderate creep pressure (10 MPa), the compression effect on the complexes is relatively mild. The degree of pore contraction is weak, with most pores appearing wedge-shaped and a few exhibiting irregular shapes (Fig. 3(f)). In the undeformed shale samples, the 'organic-clay complexes' exhibit a high degree of pore development with numerous pores. Most of these pores are irregularly shaped, with only a few appearing wedge-shaped (Fig. 3(l)). In other words, during tectonic uplift, as confining pressure decreases, the evolution of the organic pore structure in mudstone increasingly exhibits ductile rebound characteristics (Cheng et al., 2024a).

3.2. Morphological features and the development of mineral intergranular pores in shale

During diagenesis, shale is influenced by geological processes such as mineral cementation, mechanical compaction, replacement, recrystallization, and dissolution. As a result, intergranular and intragranular pores develop within and between minerals, which can be observed through SEM. Intergranular pores refer to pores that form between quartz, feldspar, and clay minerals, created by their mutual support and contact, primarily occurring between quartz particles (Fig. 4(a)–(l)). Intergranular pores exhibit various shapes, primarily irregular polygonal, wedge-shaped, angular, and slit-like. Across shale samples subjected to different creep pressure conditions, the morphology of intergranular pores remains generally consistent, with relatively more forming between quartz minerals, though their sizes vary significantly.

Under high creep pressure (20 MPa), intergranular pores are subjected to compressive stress, causing mineral fragments and clastic minerals to become tightly compacted. Some microfractures within the minerals undergo compression and closure,

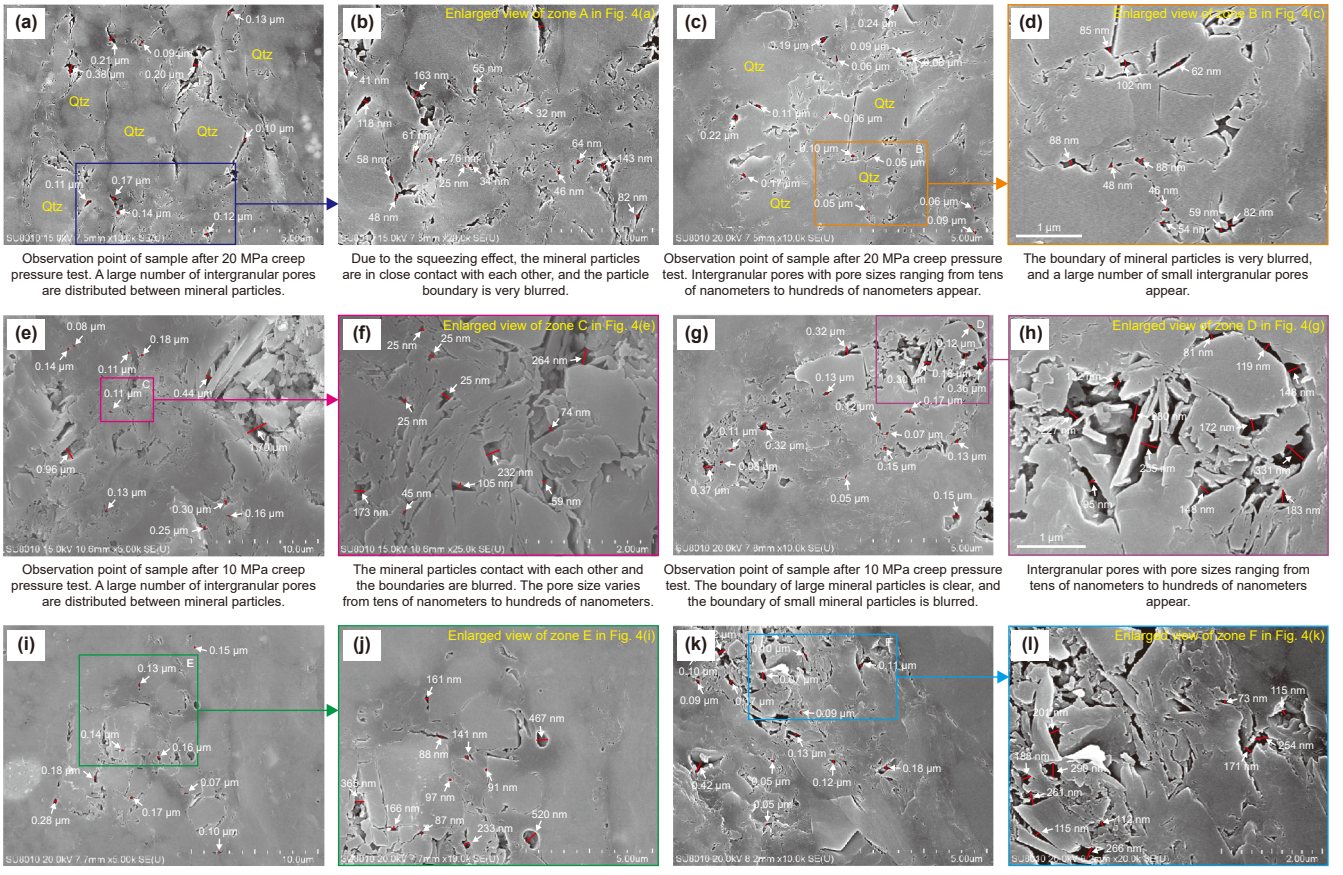

Fig. 4. Characteristics of intergranular and intragranular pores at different burial depths in longmaxi formation shale.

resulting in blurred particle boundaries. However, the elastic deformation of mineral particles allows some intergranular pores to persist. Still, under high confining pressure, intergranular pore sizes remain relatively small, mostly in the tens of nanometers range, with a few reaching up to several hundred nanometers (Fig. 4(a)–(d)). Under moderate confining pressure (10 MPa), the boundaries of mineral particles become relatively blurred, and the quantity and width of microfractures and intergranular pores between some mineral particles increase significantly. Most intergranular pores range from tens to several hundred nanometers in diameter (Fig. 4(e)–(h)). In undeformed shale samples, the boundaries of mineral particles are distinct. In some areas, intense elastic recovery occurs among mineral particles, resulting in numerous intergranular pores and microfractures, with pore sizes mostly in the hundreds of nanometers range (Fig. 4(i)–(l)). The study suggests that intergranular pores are significantly affected by mechanical compaction. As tectonic uplift occurs, the quantity and volume of intergranular pores between mineral particles and fragments increase rapidly. These intergranular pores connect to form a locally dense pore network, providing channels and space for the storage, diffusion, and migration of shale gas. In summary, during tectonic uplift, as confining pressure decreases, the evolution of intergranular pore structures in mudstone tends to exhibit brittle rebound characteristics (Cheng et al., 2024b).

Furthermore, the shale samples from the Longmaxi Formation have well-developed intragranular pores. Microscopic observations reveal that these pores mainly occur within minerals such as quartz and pyrite, predominantly as quartz dissolution pores, followed by moldic pores formed after the complete dissolution of pyrite (Fig. 4(i)–(l)). The pore shapes are primarily elliptical and quadrilateral, with sizes ranging from tens of nanometers to several micrometers. These intragranular pores generally develop in isolation, exhibiting poor or no interconnectivity, which is unfavorable for shale gas storage and migration.

3.3. Morphological characteristics and evolution patterns of microfractures in shale

SEM observations reveal that numerous microfractures are present in the Longmaxi Formation shale samples. Based on their location, these fractures can be broadly categorized into two types: microfractures within mineral particles and microfractures between mineral particles (Fig. 5). The shale samples predominantly exhibit microfractures within mineral particles. These microfractures mainly consist of those formed by the dissolution of brittle minerals, those generated by the compressive fracturing of brittle minerals, and interlayer microfractures within clay minerals.

Under high creep pressure (20 MPa), compressive deformation occurs in the interparticle fractures between brittle mineral fragments and particles, as well as in the interlayer fractures within clay minerals. However, under high confining pressure, interlayer fractures formed by clay minerals are rare, likely due to their closure under compressive stress. The initiation and propagation of microfractures between brittle mineral fragments and particles are significantly inhibited, resulting in microfractures that are

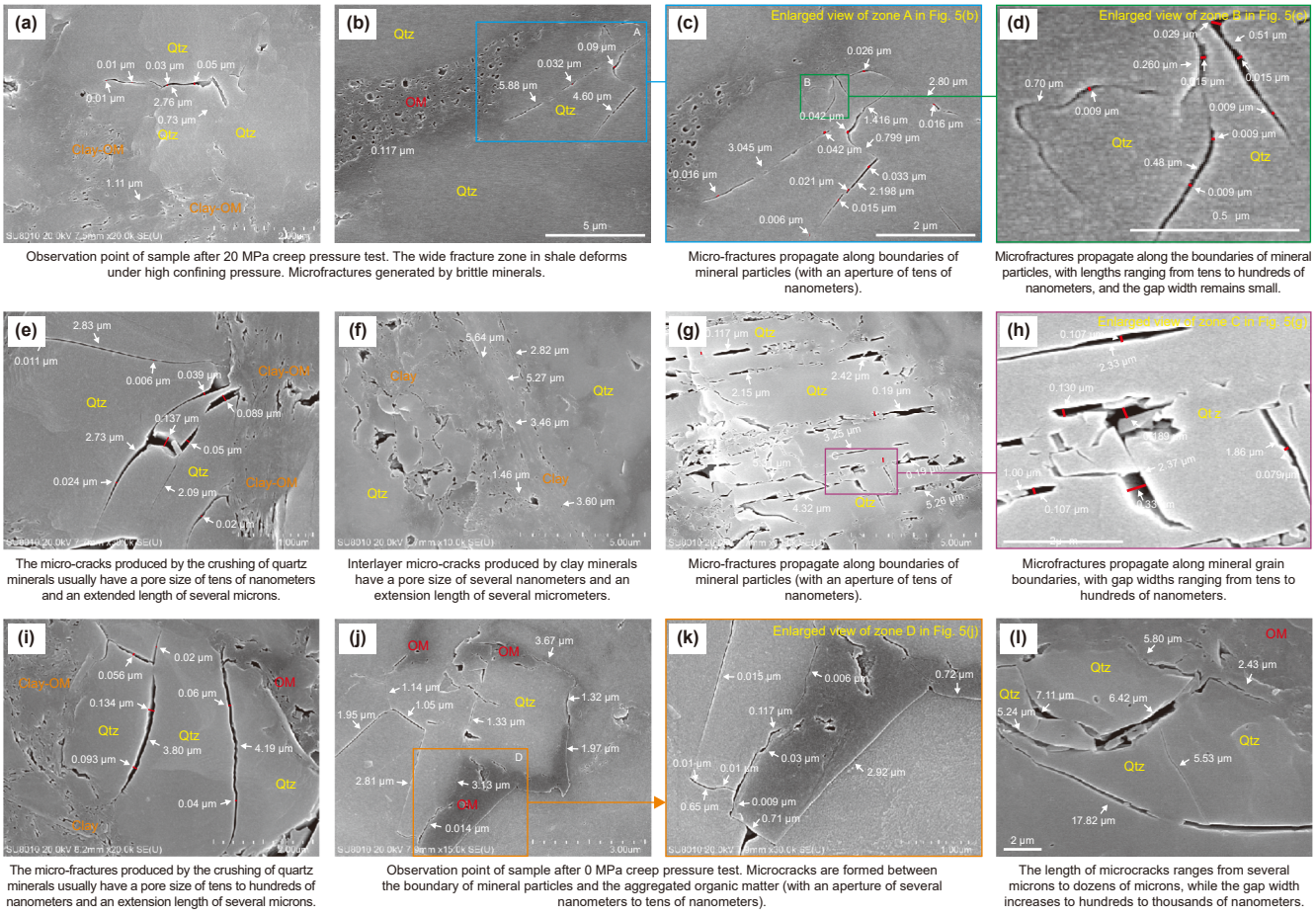

Observation point of sample after 20 MPa creep pressure test. The wide fracture zone in shale deforms under high confining pressure. Microfractures generated by brittle minerals.

Micro-fractures propagate along boundaries of mineral particles (with an aperture of tens of nanometers).

Microfractures propagate along the boundaries of mineral particles, with lengths ranging from tens to hundreds of nanometers, and the gap width remains small.

The micro-cracks produced by the crushing of quartz minerals usually have a pore size of tens of nanometers and an extended length of several microns.

Interlayer micro-cracks produced by clay minerals have a pore size of several nanometers and an extension length of several micrometers.

Micro-fractures propagate along boundaries of mineral particles (with an aperture of tens of nanometers).

Microfractures propagate along mineral grain boundaries, with gap widths ranging from tens to hundreds of nanometers.

The micro-fractures produced by the crushing of quartz minerals usually have a pore size of tens to hundreds of nanometers and an extension length of several microns.

Observation point of sample after 0 MPa creep pressure test. Microcracks are formed between the boundary of mineral particles and the aggregated organic matter (with an aperture of several nanometers to tens of nanometers).

The length of microcracks ranges from several microns to dozens of microns, while the gap width increases to hundreds to thousands of nanometers.

Fig. 5. Characteristics of microcracks and microchannels in longmaxi shale at different burial depths.

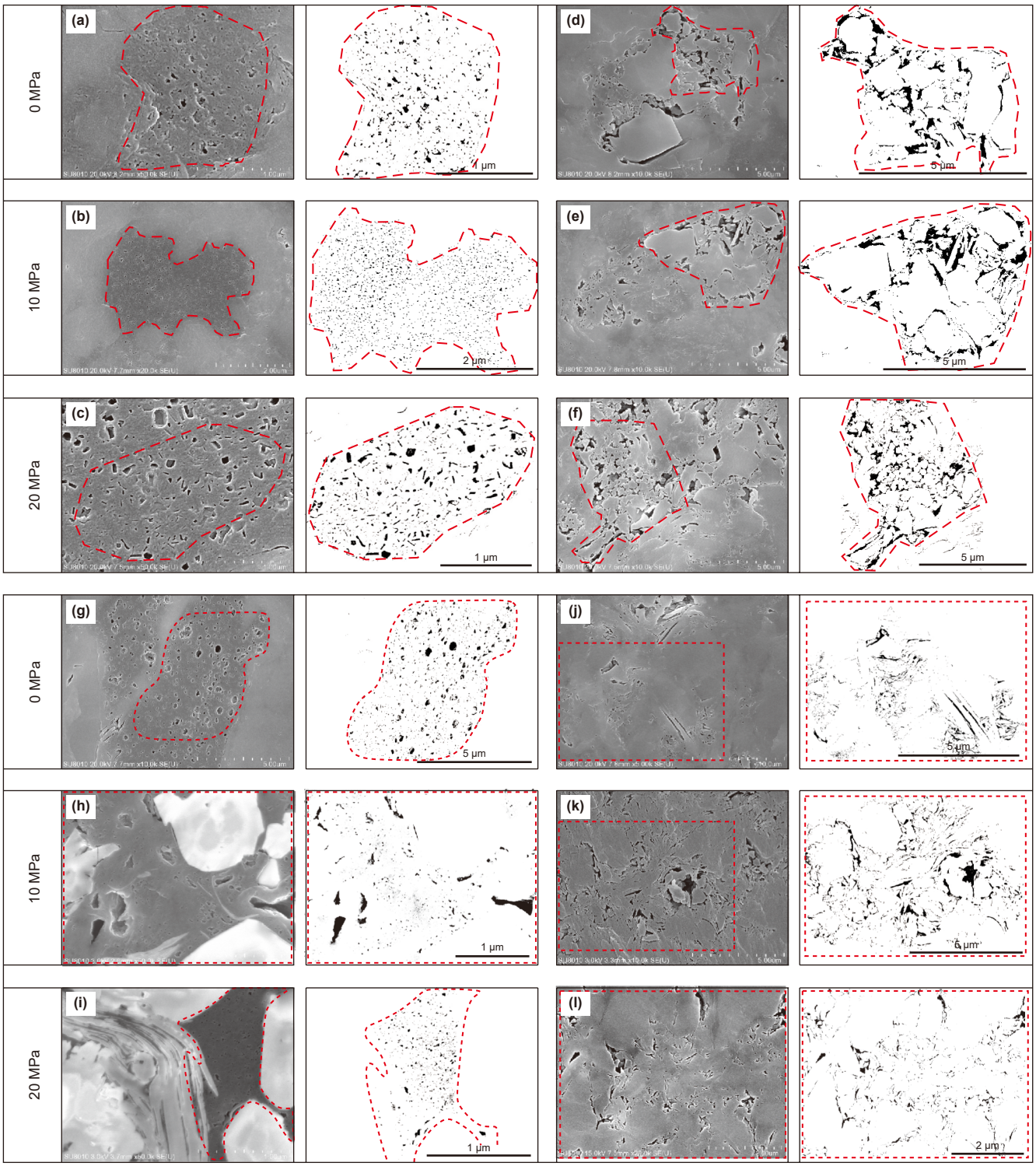

Fig. 6. Using Image-Pro Plus software, the organic matter pores and intergranular pores under different confining pressure were extracted: **(a)** TB-1, 0 MPa organic matter pores; **(b)** TB-1, 10 MPa organic matter pores; **(c)** TB-1, 20 MPa organic matter pores; **(d)** TB-1, 0 MPa intergranular pores; **(e)** TB-1, 10 MPa intergranular pores; **(f)** TB-1, 20 MPa intergranular pores; **(g)** DFA-1, 0 MPa organic matter pores; **(h)** DFA-1, 10 MPa organic matter pores; **(i)** DFA-1, 20 MPa organic matter pores; **(j)** SH-1, 0 MPa intergranular pores; **(k)** SH-1, 10 MPa intergranular pores; **(l)** SH-1, 20 MPa intergranular pores.

relatively straight, with shorter lengths (ranging from a few micrometers) and narrower widths (falling between a few and tens of nanometers) (Fig. 5(a)–(d)). Under moderate creep pressure, the microfractures formed between brittle mineral fragments and particles do not exhibit noticeable deformation or alteration, and the interlayer fractures formed by clay minerals remain clearly recognizable. Under these pressure conditions, the microfractures display a greater degree of curvature and relatively longer lengths (ranging from a few micrometers to over 10 μm). Between the micro-fractures, there are also some mineral pieces and particles, whose widths still vary from a few nanometers to tens of nanometers (Fig. 5(e)–(h)). In undeformed shale samples, the

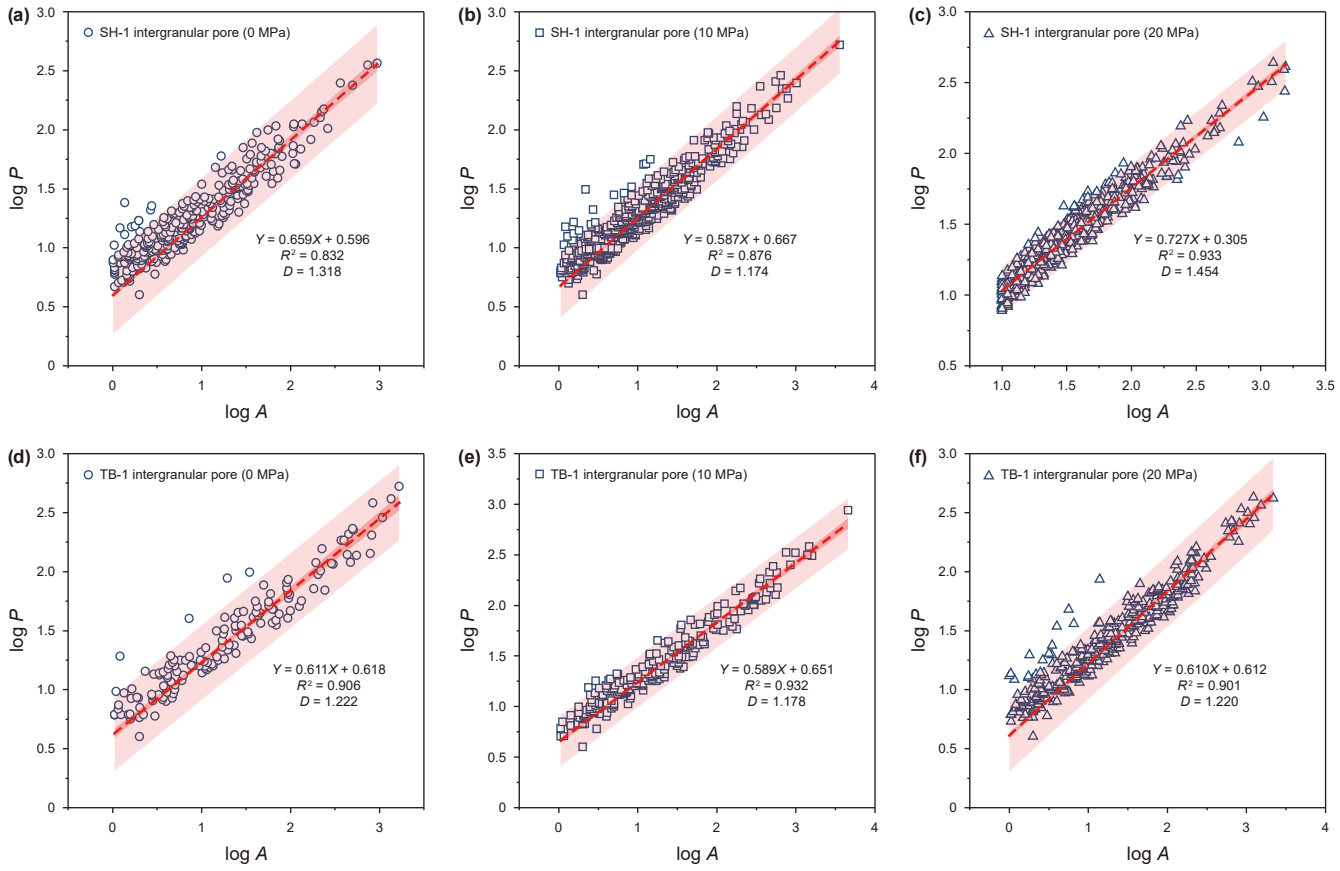

Fig. 7. The fractal relationship between the perimeter and area of intergranular pores before and after experimental deformation was calculated based on high-resolution scanning electron microscope images.

microfractures between mineral particles include both grain boundary fractures between brittle mineral particles and shrinkage fractures between organic matter and mineral particles. In the absence of pressure, these microfractures are mostly jagged and angular, with lengths ranging from a few micrometers to over 10 μm, and widths primarily in the tens of nanometers (Fig. 5(i)–(l)). Observations reveal that, in the same series of shale samples, under different triaxial creep pressure conditions, there is a trend where, as the confining pressure decreases, the length of the microfractures changes little, while the width gradually increases. Additionally, during this process, the intensity of brittle deformation between mineral particles and fragments gradually decreases, leading to the formation of numerous intergranular pores at the nano- and microscale. These pores connect with microfractures, altering the shale pore structure and thereby affecting the shale reservoir's capacity for storage, migration, and fluid flow.

4. Discussions

4.1. Pore evolution and fractal characteristics during the last tectonic uplift

The shale strata of the Longmaxi Formation have been influenced by sedimentary burial, compaction diagenesis, thermal evolution, and multiple phases of tectonic stress, leading to the development of various types of pores. This has resulted in a highly heterogeneous pore structure within the shale reservoir. The great variety of shale pore structures controls the adsorption, desorption, diffusion, migration, and storage of gases in shale reservoirs. Fractal theory has been used extensively in the investigation and characterization of pore structures and their characteristics and is a useful tool for assessing pore heterogeneity (Gao et al., 2022; Liu et al., 2023; Du et al., 2024; Sun et al., 2024; Tian et al., 2024). The complexity and dispersion properties of shale pores can be described by the fractal dimension *D*. Previous research has shown that the fractal dimension of a 2D model ranges from 1 to 2, while for a 3D model, it ranges from 2 to 3. A larger fractal dimension indicates greater pore complexity and a more random distribution (Sun et al., 2016; Feng et al., 2019; Liu et al., 2023).

Based on the above research, the Longmaxi Formation shale exhibits different morphological changes in various types of pores under different triaxial creep pressures. By utilizing high-resolution SEM images and performing image analysis, structural parameters of different types of pores, including organic pores and intergranular pores, such as pore perimeter, area, and number, were quantified. Fractal theory was further applied to calculate the fractal dimension, enabling the assessment of heterogeneity variations in shale pores under different burial conditions and exploring the rebound adjustment characteristics and patterns of shale pores influenced by the last tectonic uplift. To facilitate quick and efficient acquisition of pore structure parameters, IPP image processing software was used to capture and process SEM images, obtaining parameters such as the perimeter and area of pores in different regions and types.

Following the steps outlined above, threshold segmentation was applied to images of organic pores and intergranular pores in

shale samples under different creep pressure conditions to obtain binarized images of the pores. Subsequently, pore structure parameters for organic and intergranular pores in Longmaxi Formation shale samples from different regions and under different creep pressure conditions were extracted. Using fractal theory, the fractal dimension of the pores was calculated (Fig. 6).

The calculated fractal dimensions of organic and intergranular pores indicate that the organic and intergranular pores in Longmaxi Formation shale exhibit distinct fractal characteristics. Specifically, the fractal dimension D of organic pores ranges from 1.032 to 1.348, with correlation coefficients between 0.724 and 0.966 (Table 3; Fig. 7). The fractal dimension D of the TB and DFA sample series has a trend of first increasing and then reducing when the formation pressure drops. This suggests that organic pores' rebound adjustment during tectonic uplift is a complicated and varied process rather than a straightforward linear one. The fractal dimension D of intergranular pores ranges from 1.174 to 1.454, with correlation coefficients between 0.832 and 0.9323 (Fig. 8). As formation pressure decreases, the trend in fractal dimensions of intergranular pores is opposite to that of organic pores, showing a pattern of first decreasing and then increasing.

4.2. Organic matter pores' rebound response properties during the most recent tectonic uplift

Based on the observed morphological evolution and changes in the fractal dimension of organic pores before and after experimental deformation, this work developed an evolution model for organic pores in Longmaxi Formation shale under the impact of the most recent tectonic uplift (Fig. 9). The study suggests that under conditions of greater burial depth (high formation pressure), organic pores undergo plastic deformation due to compression. The pore shapes are predominantly slit-like, with the long axes of the pores showing a directional alignment (Fig. 3(a)–(d), Fig. 6(c) and (i) and Fig. 9(a)). Additionally, at high confining pressures, organic pores are generally smaller in scale and more uniform in shape, resulting in a lower fractal dimension of organic pores under 20 MPa creep pressure.

As tectonic uplift proceeds and the overlying formation pressure decreases, the internal gas pressure within the organic pores gradually exceeds the external formation pressure, initiating pore rebound adjustment. However, since the formation pressure is not uniform throughout the organic matter, the rebound time, rate, and degree of adjustment vary across different regions. As a result, the organic pore structures exhibit diverse and complex shapes (Fig. 3(e)–(h), Fig. 6(b) and (h)), leading to a higher fractal dimension of organic pores under 10 MPa creep pressure.

As the uplift continues and the formation pressure becomes much lower than the internal gas pressure within the organic pores, the extent of pore rebound reaches its maximum, and the organic pores cease to change. The pore structures predominantly exhibit honeycomb, beaded, or irregular shapes, with relatively uniform morphology (Fig. 3(i)–(l), Fig. 6(a) and (g); Fig. 9(b)). However, due to variations in mineral and organic content among different shale samples, especially quartz and feldspar, which influence the degree of pore compression and affect the protective role of the mineral framework, there are differences in the rebound process of organic pores. This leads to different trends in the fractal dimension of organic pores in shale samples that have not undergone experimental deformation. Among these, shale

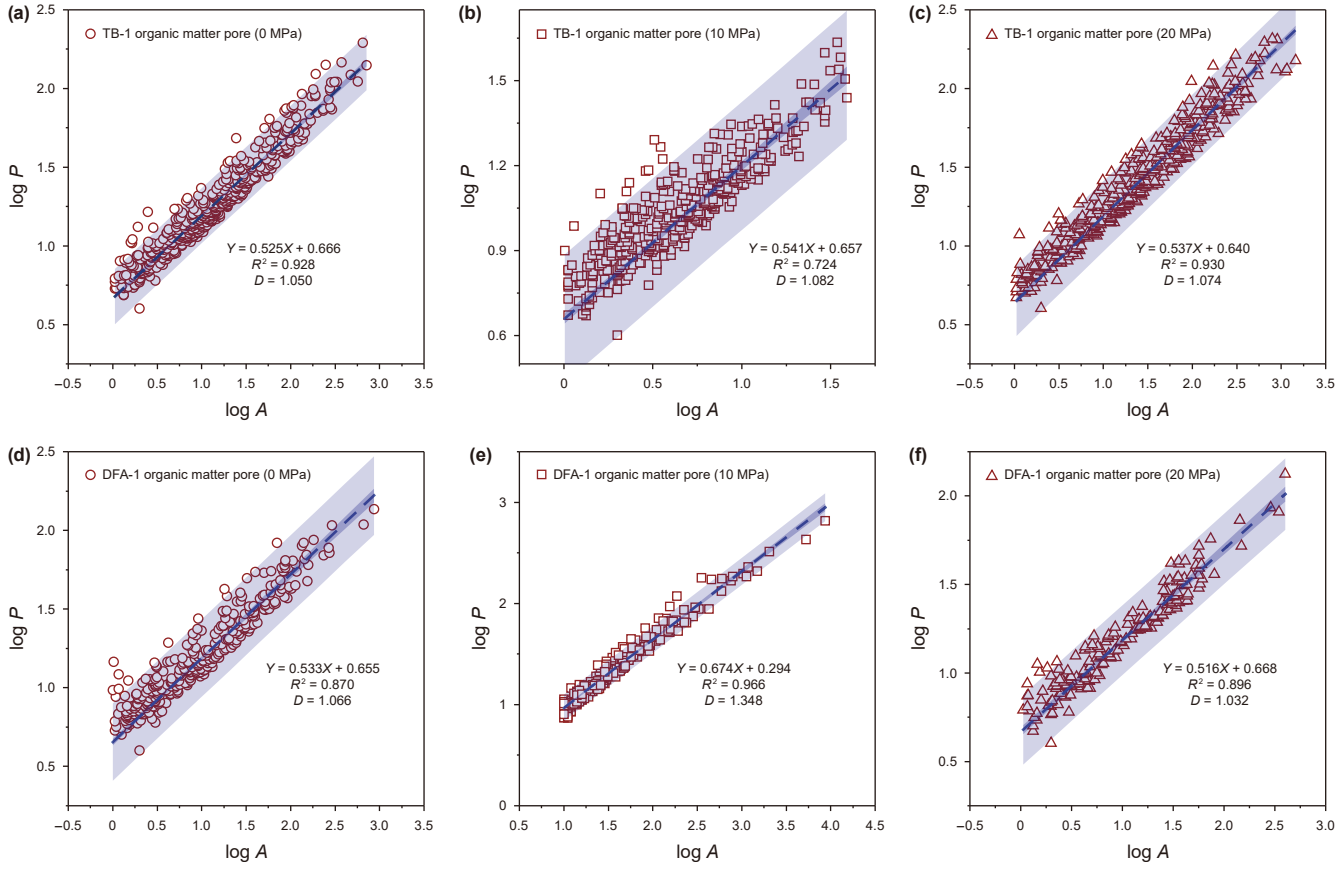

Fig. 8. The fractal relationship between the perimeter and area of organic matter pores before and after experimental deformation was calculated based on high-resolution scanning electron microscope images.

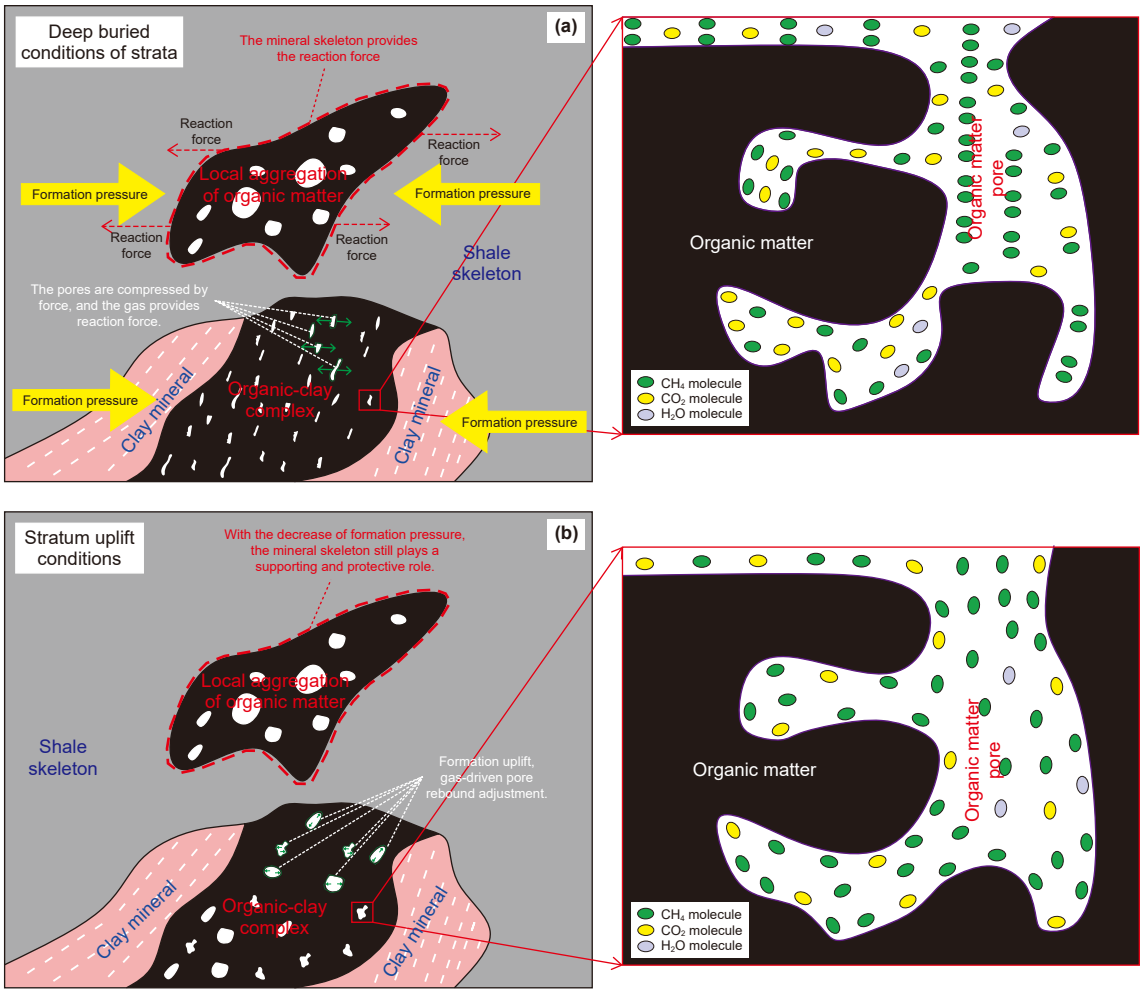

Fig. 9. Evolution pattern of organic matter pores in shale under late tectonic uplift.

samples from the Tianba and Dafengao areas (TB-1, DFA-1) have high brittle mineral content (with quartz and feldspar content exceeding 80%), which restricts the rebound evolution of organic pores, resulting in relatively uniform pore morphology (Fig. 6(a)) (Zhu et al., 2019, 2020, 2025; Shang et al., 2020; Yang et al., 2022). Consequently, the current fractal dimension of organic pores is lower. With a relatively low brittle mineral composition (below 40% for quartz and feldspar) in the Longmaxi Formation sample from the SH area (SH-1), the mineral framework's limiting influence is less pronounced. As a result, after tectonic uplift, the current fractal dimension of organic pores is higher than that of organic pores under deep burial conditions.

4.3. The rebound response characteristics of intergranular pores during the last tectonic uplift

Based on the observed morphological evolution and changes in fractal dimension of intergranular pores in Longmaxi Formation shale before and after experimental deformation, an evolution model of intergranular pores under the influence of the last tectonic uplift has been established (Fig. 10). The study suggests that intergranular pores are mainly irregular voids formed by the contact and compression of clay minerals and brittle mineral particles, with the extent of pore development being largely dependent on the relative positioning of the minerals. When the formation is buried at greater depth, high formation pressure generates strong reactive forces between mineral particles, compressing and deforming the mineral pores. This causes the rigid mineral framework to begin contracting and deforming, forming numerous, dense intergranular pores. Meanwhile, larger pores are compressed, leading to diverse and complex intergranular pore morphologies, with a relatively high fractal dimension (Fig. 4(a)–(d), Fig. 6(f) and (l), Fig. 10(a)).

As the formation pressure decreases, the reactive forces between mineral particles also decrease, allowing intergranular pores to rebound and expand. Small, dense pores that were originally present begin to connect and form relatively larger pores. However, due to the remaining formation pressure, some pores remain compressed, resulting in increased uniformity of pore morphology (Fig. 4(e)–(h), Fig. 4(e) and (k)), which leads to a relatively lower fractal dimension. When the formation pressure completely dissipates, the relative positions of mineral particles influence the extent of intergranular pore rebound, with some pores expanding more significantly. Meanwhile, other intergranular pores are restricted by the contact and compression of particles, limiting their rebound. These pores are predominantly wedge–shaped, polygonal, or irregular, resulting in decreased uniformity and a relatively higher fractal dimension (Fig. 4(i)–(l), Figs. 6(d) and 10(b)). Overall, as formation pressure increases, the fractal dimension of intergranular holes varies, and this variation is strongly correlated with the amount of brittle minerals present. The fractal dimension changes less when the brittle mineral content is high, suggesting that the intergranular pore

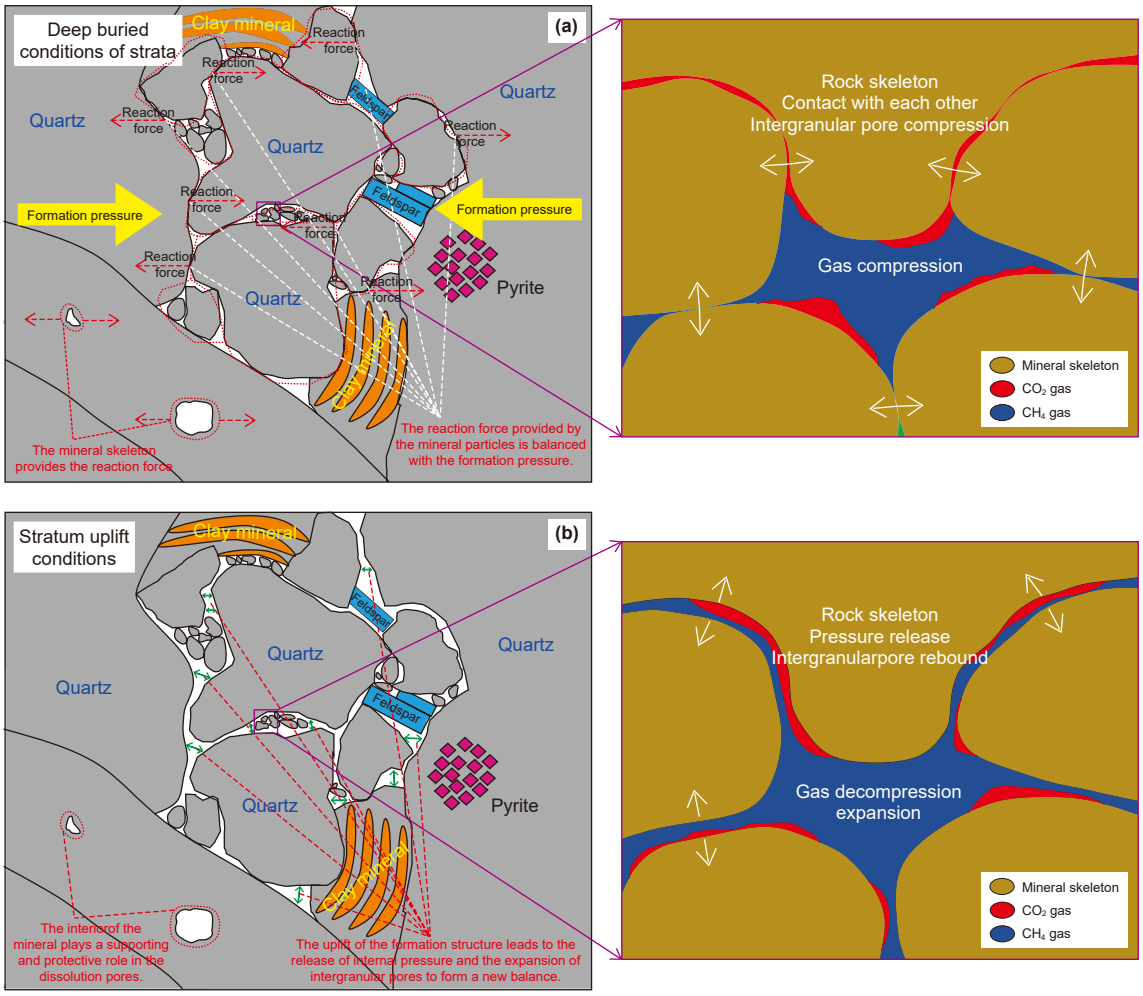

Fig. 10. Shale intergranular pore evolution model diagram of the tectonic uplift process.

structure is less elastic or more stable under formation pressure. In contrast, when the brittle mineral content is low, greater changes in fractal dimension occur, suggesting that the intergranular pore structure is more sensitive and dynamic under pressure. This indicates that the rebound evolution of intergranular pores in shale (i.e., the response of pore structure to pressure changes) is controlled by the brittle mineral content. Simply put, the higher the brittle mineral content, the less adaptive the pore structure is to pressure, while the lower the brittle mineral content, the more responsive the pore structure is to pressure changes.

4.4. Shale pore rebound response mechanism

Throughout their evolutionary history, the organic-rich shales of the Longmaxi Formation have experienced both deep burial and substantial uplift due to the numerous evolutionary cycles and periods of tectonic activity that have occurred in the Sichuan Basin and its adjacent areas (Chen et al., 2017; Liu et al., 2021; Cheng et al., 2022, 2024a). Similarly, shale pores have also undergone a complex evolutionary process. Based on previous research, the differences in pore structure evolution of experimentally deformed mud shale under various creep conditions are fundamentally the result of differing rebound evolution mechanisms across various pore types and structures.

Differential changes in organic matter pores and intergranular pores are caused by the shale's increased overburden pressure during deep burial circumstances. According to studies, the organic matter pores found in the shales of the Longmaxi Formation can be broadly divided into two categories: diffused organic matter and locally aggregated organic matter (Fig. 3). Dispersed organic matter pores protected by the mineral framework remain largely uncompressed and structurally unchanged as the overburden pressure increases, due to the effective protective role of the mineral framework. In contrast, pores within organic-clay composites experience greater load pressure than pore fluid pressure, resulting in compression and structural changes (reduction in pore size and volume). The structural characteristics of intergranular pores in shale exhibit slightly different variation patterns in response to changes in overburden pressure (Fig. 4). When the effective pressure on the intergranular pores in shale (the absolute value of the pressure differential between the pore fluid and the overburden) is less than the elastic deformation strength of the minerals, the intergranular pores undergo compression, and pore volume decreases. Conversely, if the effective pressure exceeds the mineral elastic deformation strength, the minerals fracture, leading to damage in the pore structure.

In light of the study above, this study hypothesizes that the rebound adjustment of shale pores can be broadly categorized into two pathways: one associated with organic matter, clay, or other plastic mineral pores, and the other with intergranular pores formed by minerals such as quartz and feldspar (Fig. 11). When organic-rich shale undergoes a relatively stable uplift process and is

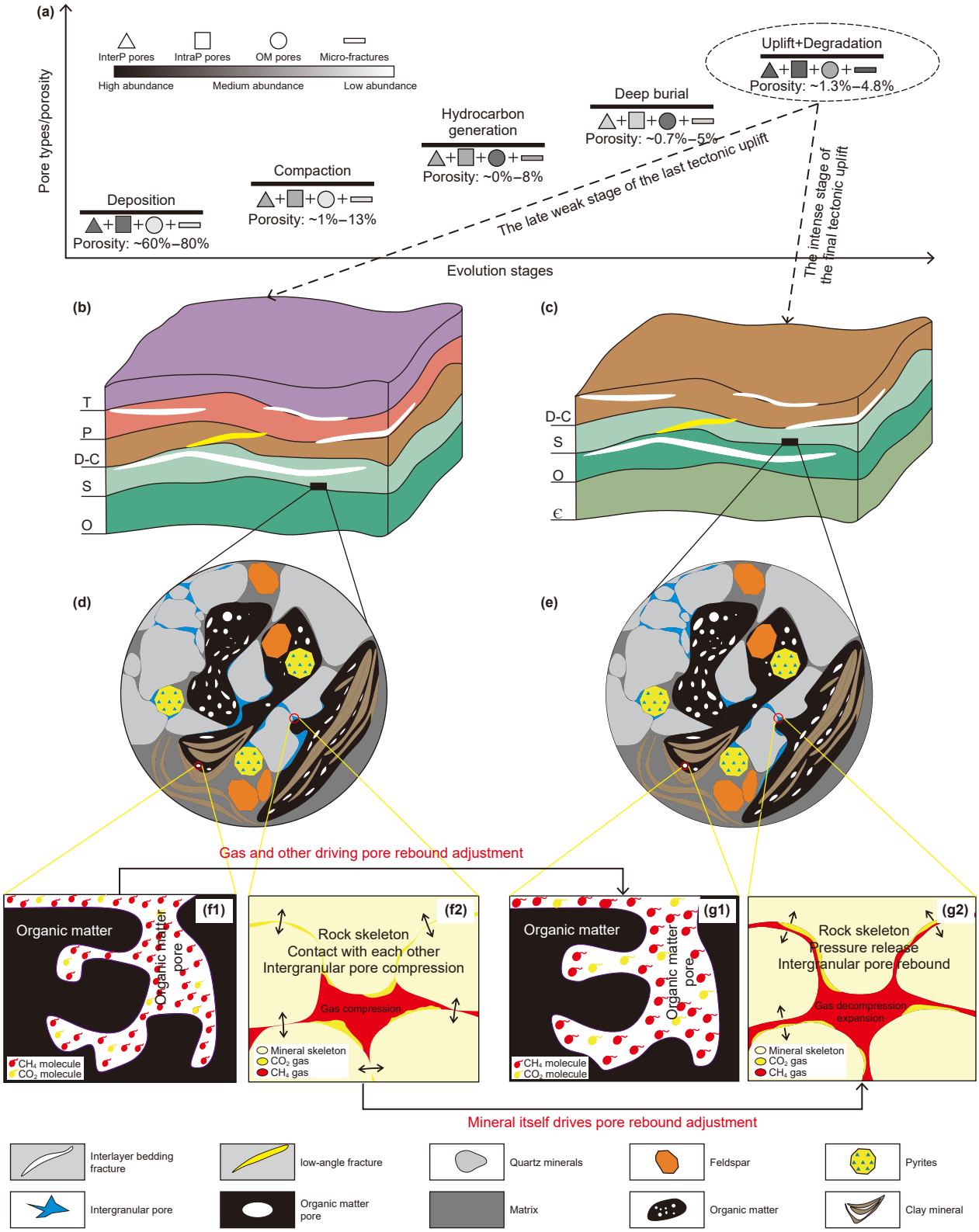

Fig. 11. **(a)** Schematic diagram illustrating the main stages of shale deposition, burial, and uplift, and their relationship with the development of shale pore types and abundance (modified from Zhu et al., 2019). **(b, c)** Comprehensive stratigraphic conceptual diagrams (modified from Yang et al., 2022). **(d, e)** Conceptual diagrams showing mineral and organic matter development in Longmaxi Formation shale under the microscope. **(f, g)** Conceptual diagrams of shale pore rebound response mechanisms.

not affected by intense subsequent tectonic activity, with favorable conditions for shale gas preservation, a significant amount of gas (such as CH_4, CO_2, etc.) within the organic matter pores can lead to an overpressure state in some of these pores. As tectonic uplift occurs and the overlying strata erode, the overburden pressure becomes less than the fluid pressure within the organic matter pores in the shale. This leads to an increase in the pressure coefficient of gases like CH_4 and CO_2 within the pores of plastic minerals such as organic matter. The gas expands, and diffusion pressure acts as a driving force, prompting the rebound adjustment of organic matter pores (Fig. 11(f1) and (g1)). Additionally, as tectonic uplift proceeds and the overlying strata erode, the overburden pressure becomes less than the mineral deformation strength and the supporting forces between mineral particles in intergranular pores formed by minerals such as quartz and feldspar. This allows for the elastic recovery of the mineral particles, causing the compressed pores to undergo rebound adjustment, resulting in changes to the pore structure (Fig. 11(f2) and (g2)).

Therefore, moderate tectonic uplift can enhance the connectivity of shale reservoirs, improving seepage and diffusion capacity, which accelerates the adsorption and desorption rates of shale gas. However, if the tectonic uplift is too intense, it can weaken the adsorption capacity of the shale, leading to the formation of well-connected network microfractures. These microfractures can connect with pores and macroscopic fractures, causing shale gas to escape and negatively impacting its storage and retention in the reservoir.

4.5. Insights into the development of marine shale gas in the Sichuan Basin

The differentiated rebound behavior of various pore types in the shale reservoir during the final stratigraphic uplift reveals the nonlinear characteristics of pore structure evolution and its complex regulatory mechanisms for shale gas occurrence and migration. The variation patterns of fractal dimensions and their interactions across different pore types provide multi-scale theoretical support for reservoir evaluation and the optimization of development strategies.

The aforementioned study indicates that the fractal dimension of intergranular pores first decreases and then increases with stratigraphic uplift. During the stage of weak final tectonic uplift (The formation depth remains greater than 1000 m), the reduction in overlying strata pressure promotes brittle rebound of intergranular pores, leading to the expansion of pore throats, a reduction in surface roughness, and an enhancement of pore permeability (Li et al., 2021; Shi et al., 2023) (Fig. 11(b)–(d), (f) and (g)). As the degree of uplift intensifies (The formation depth is less than 1000 m), the rearrangement of shale mineral particles increases the roughness of pore edges, leading to a rise in fractal dimension, an increase in the tortuosity of pore flow paths, and the possible formation of heterogeneous flow barriers locally (Shi et al., 2023) (Fig. 11(c)–(e), (f), and (g)). Additionally, the fractal dimension of organic matter pores first increases and then decreases with stratigraphic uplift. During the stage of weak final tectonic uplift (The formation depth remains greater than 1000 m), organic matter pores undergo plastic rebound adjustment, increasing pore surface complexity and enhancing gas storage capacity. As tectonic uplift intensifies (the formation depth is less than 1000 m), organic matter pore throats merge, and connectivity increases, leading to a simplified pore structure. The adsorption–desorption rate and diffusion efficiency improve synchronously (Cheng et al., 2024a). At the same time, with the uplift of strata, the complexity of microfracture networks increases, leading to a reduction in the effective storage space of the shale (Sari et al., 2022). The coupled effect of these three factors significantly impacts the flow-storage balance in the shale reservoir. Furthermore, the flow advantage period of intergranular pores and the storage advantage period of organic matter pores are temporally and spatially consistent. This is evident during moderate stratigraphic uplift (the formation depth remains greater than 1000 m), when the shale reservoir forms a "high permeability-high gas storage" coupling zone. However, when stratigraphic uplift becomes excessive (the formation depth is less than 1000 m), it may trigger disordered expansion between organic pores, intergranular pores, microfractures, and fractures, leading to compression of effective storage space and gas dissipation.

Therefore, moderate stratigraphic uplift helps improve the connectivity and gas storage capacity of the shale reservoir, enhances its permeability and diffusion capabilities, and accelerates the adsorption and desorption rates of shale gas. However, when the degree of stratigraphic uplift becomes excessive, it weakens the shale's adsorption capacity, forming a network of microfractures with good connectivity that connects with pores and fractures, leading to rapid gas dissipation. Determining suitable burial depth conditions can, to some extent, enhance the shale's storage capacity and connectivity, which has practical significance for shale gas accumulation and the optimal development of sweet spots.

5. Conclusion

The study used fractal theory analysis, argon ion beam polishing, and Ar-SEM on shale samples from various regions that were all disclosed to the same experimental conditions before and after deformation in order to uncover the evolutionary mechanisms of shale pores and the patterns of rebound response under the influence of the most recent tectonic uplift. This research effectively eliminated the interference of non-deformation factors in the analysis of pore structure evolution by using freshly extracted outcrop samples for triaxial creep experiments, in contrast to previous studies. Additionally, the shale samples had the same initial pore structures and organic geochemical characteristics before the triaxial creep experiments. Consequently, the rebound response of the pore structure can be used to explain the variations in pore structure between the shale samples before and after the creep trials. The following is a summary of the primary findings:

(1) The Longmaxi Formation shale exhibits extensive development of intergranular and intragranular pores, organic pores, and microfractures, providing ample storage space for shale gas. As the creep pressure decreases, organic pores affected by compaction gradually undergo rebound adjustments, with increasing complexity and distribution characteristics that initially grow and then decrease, leading to an increase in pore quantity. As the creep pressure decreases, intergranular pores show a trend of increasing complexity and distribution, improving rebound and enlarging pore shapes. Microfractures, with the decrease in formation pressure, experience reactivation and expansion, becoming more developed with enhanced connectivity.
(2) Differences in the rebound evolution mechanisms of distinct pore types and structures are mainly the cause of the variances in the pore structure evolution of experimentally deformed shale under various creep settings. Based on microscopic evolution and fractal dimension variation characteristics, it is inferred that shale pore rebound adjustment generally follows two pathways: one involving organic pores or clay-rich plastic mineral pores, and the other involving intergranular pores formed by minerals such

as quartz and feldspar. The driving forces in their rebound evolution primarily include the diffusion pressure of CH_4, CO_2, and other gases under overpressure conditions, as well as the deformation strength of quartz, feldspar, and the supporting forces between mineral grains.

This study has some limitations. First and foremost, the experimental deformation circumstances do not take into consideration the effects of differential stress and temperature on the evolution of pore structure; instead, they only take into account the effect of confining pressure on shale pore structure. In future research, we will incorporate control experiments with varying stress and temperature conditions to more closely mimic real geological conditions, thereby investigating the shale pore rebound and evolution process in greater detail. Additionally, this study provides a qualitative and semi-quantitative analysis of pore rebound and evolution mechanisms based on Ar-ion polishing, SEM observation, and fractal theory. However, it lacks a fully quantitative perspective. Therefore, in future research, we will employ quantitative analysis patterns to enhance our understanding of deformation characteristics and pore structure variations in experimentally deformed shale samples, addressing the limitations and shortcomings of the current study.

CRediT authorship contribution statement

Yang Wang: Methodology, Formal analysis, Writing – original draft, Investigation, Conceptualization. **Han-Yu Zhang:** Writing – review & editing, Data curation, Software. **Yan-Ming Zhu:** Supervision, Writing – review & editing, Conceptualization. **Hao-Ran Chen:** Conceptualization, Writing – review & editing. **Zhi-Xuan Wang:** Data curation. **Jia-Le Li:** Data curation.

Data availability

Data will be made available on request.

Declaration of competing interest

The authors declare that they have no known competing financial interests or personal relationships that could have appeared to influence the work reported in this paper.

Acknowledgement

This study was supported by the Natural Science Foundation of China (Grant No. 42172156, 42472222), the Fundamental Research Funds for the Central Universities (Grant No. 2022YCPY0201).

Appendix A. Supplementary data

Supplementary data to this article can be found online at https://doi.org/10.1016/j.petsci.2025.09.016.

References

Cai, X.Y., Zhou, D.H., Zhao, P.R., et al., 2023. Development progress and outlook of deep and normal pressure shale gas of SINOPEC. Petrol. Explor. Dev. 45 (6), 1039–1049. https://doi.org/10.11781/sysydz2023061039 (in Chinese).

Chai, B.Q., Zhao, F., Ji, Y.B., et al., 2023. Lithofacies types and reservoir characteristics of mountain shale in Wufeng Formation-Member 1 of Longmaxi Formation in the complex structural area of northern Yunnan–Guizhou. ACS Omega 8 (2), 2085–2097. https://doi.org/10.1021/acsomega.2c05868.

Chaturvedi, K.R., Sharma, T., 2022. Modified smart water flooding for promoting carbon dioxide utilization in shale-enriched heterogeneous sandstone under surface conditions for oil recovery and storage prospects. Environ. Sci. Pollut. Control Ser. 29, 41788–41803. https://doi.org/10.1007/s11356-022-18851-6.

Chen, J.Q., Jiang, F.J., Cong, Q., et al., 2023. Adsorption characteristics of shale gas in organic–inorganic slit pores. Energy 278, 127788. https://doi.org/10.1016/j.energy.2023.127788.

Chen, S.B., Zhu, Y.M., Chen, S., et al., 2017. Hydrocarbon generation and shale gas accumulation in the Longmaxi Formation, southern Sichuan Basin, China. Mar. Petrol. Geol. 86, 248–258. https://doi.org/10.1016/j.marpetgeo.2017.05.017.

Cheng, G.J., Liu, G.N., Ye, D.Y., et al., 2024a. A multi-scale fractal model of gas flow considering the evolution of kerogen microstructure and the multi-physical coupling. Comput. Geotech. 165, 105873. https://doi.org/10.1016/j.compgeo.2023.105873.

Cheng, G.X., Jiang, B., Li, F.L., et al., 2022. Distribution prediction of shale deformation structures in tectonically complex area based on relationship between geological structures and shale deformation. Front. Earth Sci. 10, 813074. https://doi.org/10.3389/feart.2022.813074.

Cheng, G.X., Jiang, B., Li, F.L., et al., 2024b. Evolution mechanism of pore structures of organic–rich shale under tectonic deformation: A comparative study between whole rock and kerogen samples. Nat. Resour. Res. 33 (1), 263–297. https://doi.org/10.1007/s11053-023-10283-4.

Cheng, G.X., Wu, C.F., Jiang, B., et al., 2024a. Pore structure evolution of organic–rich shale induced by structural deformation based on shale deformation experiments. Energy 306, 132463. https://doi.org/10.1016/j.energy.2024.132463.

Dong, W.Q., 2018. Effects of temperature and effective stress on stress sensitivity of shale reservoirs. Petrochem. Indust. Appl. 37 (3), 62–66. https://doi.org/10.3969/j.issn.1673-5285.2018.03.014 (in Chinese).

Du, M., Yang, Z.M., Lv, W., et al., 2024. Experimental study on microscopic production characteristics and influencing factors during dynamic imbibition of shale reservoir with online NMR and fractal theory. Energy 310, 133244. https://doi.org/10.1016/j.energy.2024.133244.

Feng, G.J., Zhu, Y.M., Chen, S.B., et al., 2020. Supercritical methane adsorption on shale over wide pressure and temperature ranges: Implications for gas-in-place estimation. Energy Fuel 34 (3), 3121–3134. https://doi.org/10.1021/acs.energyfuels.9b04498.

Feng, G.J., Zhu, Y.M., Wang, G.X., et al., 2019. Supercritical methane adsorption on overmature shale: Effect of pore structure and fractal characteristics. Energy Fuel 33 (9), 8323–8337. https://doi.org/10.1021/acs.energyfuels.9b01857.

Gao, B., Wu, C.F., Song, Y., et al., 2022. Effects of coalification on nano–micron scale pore development: From bituminous to semi–anthracite. J. Nat. Gas Sci. Eng. 105, 104681. https://doi.org/10.1016/j.jngse.2022.104681.

Gentzis, T., 2016. Review of the hydrocarbon potential of the steele shale and Niobrara formation in Wyoming, USA: A major unconventional resource play? Int. J. Coal Geol. 166, 118–127. https://doi.org/10.1016/j.coal.2016.07.002.

Gu, Z.D., Wang, X., Nunns, A., et al., 2021. Structural styles and evolution of a thin-skinned fold and thrust belt with multiple detachments in the eastern Sichuan Basin, South China. J. Struct. Geol. 142, 104191. https://doi.org/10.1016/j.jsg.2020.104191.

Guo, J.Y., Li, M., Zhang, M.W., et al., 2023. Rock physics model for velocity—pressure relations and its application to shale pore pressure estimation. Petrol. Explor. Dev. 50 (2), 404–418. https://doi.org/10.1016/S1876-3804(23)60396-9.

Guo, X.S., Wang, R.Y., Shen, B.J., et al., 2025. Geological characteristics, resource potential, and development direction of shale gas in China. Petrol. Explor. Dev. 52 (1), 17–32. https://doi.org/10.1016/S1876-3804(11)60001-3.

Guo, X.S., Hu, D.F., Huang, R.C., et al., 2020. Deep and ultra-deep natural gas exploration in the Sichuan Basin: Progress and prospect. Nat. Gas. Ind. 7 (5), 419–432. https://doi.org/10.3787/j.issn.1000-0976.2020.05.001.

Han, X.J., Fan, C.Y., Gao, C., et al., 2023. Restoration method of disequilibrium compaction overpressure in tectonically uplifted area: A case study of Yanchang formation in Xiasiwan area, Ordos Basin. Nat. Gas Geosci. 34 (7), 1163–1172. https://doi.org/10.11764/j.issn.1672-1926.2023.02.008 (in Chinese).

Li, J., Li, H., Jiang, W., et al., 2024. Shale pore characteristics and their impact on the gas-bearing properties of the Longmaxi formation in the Luzhou area. Sci. Rep. 14 (1), 16896. https://doi.org/10.1038/s41598-024-66759-7.

Li, X.S., Zhu, H.J., Zhang, K.X., et al., 2021. Pore characteristics and pore structure deformation evolution of ductile deformed shales in the Wufeng–Longmaxi Formation, Southern China. Mar. Petrol. Geol. 127, 104992. https://doi.org/10.1016/j.marpetgeo.2021.104992.

Li, X.Y., Chen, S.B., Wu, J.F., et al., 2024. Dynamic variation of full–scale pore compressibility and heterogeneity in deep shale gas reservoirs: Implications for pore system preservation. Energy Fuel 38 (5), 3880–3899. https://doi.org/10.1021/acs.energyfuels.3c04097.

Liu, J., Zhu, Y.M., Shang, F.H., et al., 2023. Pore system diversity and control factors of high-overmature shale: Taking the Lujiaping and Longmaxi Formation shales as an example. Energy Fuel 37 (13), 9047–9065. https://doi.org/10.1021/acs.energyfuels.3c00687.

Liu, S.G., Deng, B., Li, Z.W., et al., 2012. Architectures of basinmountain systems and their influences on gas distribution: A case study from Sichuan Basin, South China. J. Asian Earth Sci. 47, 204–215. https://doi.org/10.1016/j.jseaes.2011.10.012.

Liu, S.G., Yang, Y., Deng, B., et al., 2021. Tectonic evolution of the Sichuan Basin, Southwest China. Earth Sci. Rev. 213, 103470. https://doi.org/10.1016/j.earscirev.2020.103470.

Liu, W.X., Lu, L.F., Wei, Z.H., et al., 2020. Microstructure characteristics of Wufeng–Longmaxi shale gas reservoirs with different depth, southeastern Sichuan Basin. Petrol. Geol. Exp. 42 (3), 378–386. https://doi.org/10.11781/sysydz202003378 (in Chinese).

Long, S.X., Feng, D.J., Li, F.X., 2018. Prospect of the deep marine shale gas exploration and development in the Sichuan Basin. Nat. Gas Geosci. 29 (4), 443–451. https://doi.org/10.1016/j.jnggs.2018.11.001.

Meng, Q.R., Wang, E.C.E., Hu, J.M., 2005. Mesozoic sedimentary evolution of the northwest Sichuan Basin: Implication for continued clockwise rotation of the South China block. Geol. Soc. Am. Bull. 117 (1), 396–410. https://doi.org/10.1130/B25407.

Milliken, K.L., Day–Stirrat, R.J., Papazis, P.K., et al., 2012. Carbonate Lithologies of the Mississippian Barnett Shale, Fort Worth Basin, Texas. Shale reservoirs-giant Resources for the 21st Century: AAPG Memoir97. American Association of Petroleum Geologists, Tulsa, pp. 290–321. https://doi.org/10.1306/13321473M97252.

Nie, H.K., He, Z.L., Liu, G.X., et al., 2020. Status and direction of shale gas exploration and development in China. J. China Inst. Min. Technol. 49 (1), 13–35. https://doi.org/10.1021/acs.energyfuels.0c04131.

Sari, M., Sarout, J., Poulet, T., et al., 2022. The brittle–ductile transition and the formation of compaction bands in the Savonnières limestone: Impact of the stress and pore fluid. Rock Mech. Rock Eng. 55 (11), 6541–6553. https://doi.org/10.1007/s00603-022-02963-z.

Shang, F.H., Zhu, Y.M., Gao, H.T., et al., 2020. Relationship between tectonism and composition and pore characteristics of shale reservoirs. Geofluids 2020 (1), 9426586. https://doi.org/10.1155/2020/9426586.

Shi, X.W., Liang, Z.K., Yang, Y.R., et al., 2023. Tectonic control on shale pore structure and gas content from the longmaxi Formation shale in southern Sichuan Basin, China: Insights from fractal analysis and low-pressure gas adsorption. Processes 11 (10), 2873. https://doi.org/10.3390/pr11102873.

Shi, Z.S., Wang, H.Y., Sun, S.S., et al., 2021. Graptolite zone calibrated stratigraphy and topography of the late Ordovician–early Silurian Wufeng–Lungmachi shale in upper Yangtze area, South China. Arabian J. Geosci. 14, 213. https://doi.org/10.1007/s12517-021-06517-5.

Sun, H.Q., Cai, X.Y., Hu, D.G., et al., 2023. Theory, technology and practice of shale gas three-dimensional development: A case study of Fuling shale gas field in Sichuan Basin, SW China. Petrol. Explor. Dev. 50 (3), 573–584. https://doi.org/10.1016/S1876-3804(23)60417-3.

Sun, M.D., Yu, B.S., Hu, Q.H., et al., 2016. Nanoscale pore characteristics of the Lower Cambrian Niutitang Formation shale: A case study from well yuke #1 in the southeast of Chongqing, China. Int. J. Coal Geol. 154–155, 16–29. https://doi.org/10.1016/j.coal.2015.11.015.

Sun, S.S., Shi, Z.S., Dong, D.Z., et al., 2024. Formation and evolution of shale overpressure in deep Wufeng-Longmaxi Formation in southern Sichuan basin and its influence on reservoir pore characteristics. Front. Earth Sci. 12, 1375241. https://doi.org/10.3389/feart.2024.1375241.

Sun, W.J.B., Zuo, Y.J., Wen, Z.J., et al., 2024. The impact of pore heterogeneity on pore connectivity and the controlling factors utilizing spontaneous imbibition combined with multifractal dimensions: Insight from the Longmaxi Formation in Northern Guizhou. Energy 311, 133329. https://doi.org/10.1016/j.energy.2024.133329.

Sun, Y.F., 2004. Pore structure effects on elastic wave propagation in rocks: AVO modelling. J. Geophys. Eng. 1 (4), 268–276. https://doi.org/10.1088/1742-2132/1/4/005.

Tenger, B., Shen, B.J., Yu, L.J., et al., 2017. Mechanisms of shale gas generation and accumulation in the Ordovician Wufeng-Longmaxi Formation, Sichuan Basin, SW China. Petrol. Explor. Dev. 44 (1), 69–78. https://doi.org/10.1016/S1876-3804(17)30009-5.

Tian, X., Duan, X.G., Sun, M.D., et al., 2024. Evolution of fractal characteristics in shales with increasing thermal maturity: Evidence from neutron scattering, N_2 physisorption, and FE-SEM imaging. Energy 298, 131342. https://doi.org/10.1016/j.energy.2024.131342.

Voss, R.F., Laibowitz, R.B., Alessandrini, E.I., 1991. Fractal geometry of percolation in thin gold Films//scaling phenomena. In: Disordered Systems. Springer US, pp. 279–288.

Wang, H.J., Chen, S.B., Zhang, S.J., et al., 2023. Study on fracture characteristics in coal and shale for coal–measure gas reservoir based on 3D CT reconstruction and fractal features. Front. Earth Sci. 17, 514–526. https://doi.org/10.1007/s11707-022-1027-9.

Wang, X.L., Pan, J.N., Wang, K., et al., 2022. Fracture variation in high-rank coal induced by hydraulic fracturing using X-ray computer tomography and digital volume correlation. Int. J. Coal Geol. 252, 103942. https://doi.org/10.1016/j.coal.2022.103942.

Wei, G., Jia, D., Yang, W., et al., 2019. Structural Characteristics, Oil and Gas in Sichuan Basin. Science Press, Beijing (in Chinese).

Xiang, J., Zhu, Y.M., Wang, Y., et al., 2022. Structural deformation and its pore-fracture system response of the Wufeng-Longmaxi shale in the Northeast Chongqing area, using FE-SEM, gas adsorption, and SAXS. J. Petrol. Sci. Eng. 209, 109877. https://doi.org/10.1016/j.petrol.2021.109877.

Xiang, M., Xu, S., Wen, Y.R., et al., 2024. Influence of tectonic preservation conditions on the nanopore structure of shale reservoir: A case study of Wufeng-Longmaxi Formation shale in Western Hubei area, South China. Pet. Sci. 21 (4), 2203–2217. https://doi.org/10.1016/j.petsci.2024.02.008.

Xu, H., Zhang, J.F., Tang, D.Z., et al., 2012. Controlling factors of underpressure reservoirs in the Sulige gas field, Ordos Basin. Petrol. Explor. Dev. 39 (1), 64–68.. https://doi.org/10.1016/S1876-3804(12)60016-0 (in Chinese).

Xu, Q.C., Wang, H.Z., Guo, R.L., et al., 2022. Pore structural characteristics and methane adsorption capacity of transitional shale of different depositional and burial processes: A case study of shale from Taiyuan Formation of the Southern North China Basin. J. Pet. Explor. Prod. Technol. 12, 995–1008. https://doi.org/10.1007/s13202-021-01359-z.

Yang, L., Yang, D., Li, Y.X., et al., 2024. Nanoindentation study on microscopic mineral mechanics and bedding characteristics of continental shales. Energy 312, 133614. https://doi.org/10.1016/j.energy.2024.133614.

Yang, W., Wang, Y.H., Du, W., et al., 2022. Behavior of organic matter-hosted pores within shale gas reservoirs in response to differential tectonic deformation: Potential mechanisms and innovative conceptual models. J. Nat. Gas Sci. Eng. 102, 104571. https://doi.org/10.1016/j.jngse.2022.104571.

Yin, J., Wei, L., Sun, S.S., et al., 2023. Overpressure generation and evolution in deep Longmaxi Formation shale reservoir in Southern Sichuan Basin: Influences on pore development. Energies 16 (6), 2533. https://doi.org/10.3390/en16062533.

Yu, W.M., Yuan, S.S., Tang, H.X., et al., 2024. The effect of structural preservation conditions on pore structure of marine shale reservoir: A case study of the Wufeng-Longmaxi Formation shale, southern Sichuan Basin, China. Front. Earth Sci. 12, 1360202. https://doi.org/10.3389/feart.2024.1360202.

Zeng, Y.J., Chen, Z., Bian, X.B., 2016. Breakthrough in staged fracturing technology for deep shale gas reservoirs in SE Sichuan Basin and its implications. Nat. Gas. Ind. 3 (1), 45–51. https://doi.org/10.1016/j.ngib.2016.02.005.

Zhang, F.Q., Sun, Y., Lu, S.Y., et al., 2023. Characteristics of pressure relief induced by shale brittle fracture in tectonic uplift area and its influence on shale oil enrichment: A case study of Chang 7, sub-member of Yanchang Formation in Yan'an area. Petrol. Geol. Exp. 45 (5), 936–951.. https://doi.org/10.11781/sysydz202305936 (in Chinese).

Zhang, S.J., Sang, Q., Dong, M.Z., 2021. Experimental study of pressure sensitivity in shale rocks: Effects of pore shape and gas slippage. J. Nat. Gas Sci. Eng. 89, 103885. https://doi.org/10.1016/j.jngse.2021.103885.

Zhu, H.J., Ju, Y.W., Huang, C., et al., 2020. Microcosmic gas adsorption mechanism on clay-organic nanocomposites in a marine shale. Energy 197, 117256. https://doi.org/10.1016/j.energy.2020.117256.

Zhu, H.J., Ju, Y.W., Lu, Y.J., et al., 2025. Natural evidence of organic nanostructure transformation of shale during bedding-parallel slip. Geol. Soc. Am. Bull. 137 (5–6), 2719–2746. https://doi.org/10.1130/B37712.1.

Zhu, H.J., Ju, Y., Huang, C., et al., 2019. Pore structure variations across structural deformation of Silurian Longmaxi shale: An example from the Chuandong thrust–fold belt. Fuel 241, 914–932. https://doi.org/10.1016/j.fuel.2018.12.108.

Zou, C.N., Lin, M.J., Ma, F., et al., 2024. Development, challenges and strategies of natural gas industry under carbon neutral target in China. Petrol. Explor. Dev. 51 (2), 476–497. https://doi.org/10.1016/S1876-3804(24)60038-8.

Zou, C.N., Zhao, Q., Wang, H.Y., et al., 2022. The main characteristics of marine shale gas and the theory & technology of exploration and development in China. Nat. Gas. Ind. B 42 (8), 1–13. https://doi.org/10.3787/j.issn.1000-0976.2022.08.001 (in Chinese).